

First detection of the moving lens effect with ACT and DESI LS

Selim C. Hotinli,^{1,*} Kendrick M. Smith,¹ Simone Ferraro,^{2,3} Ali Beheshti,^{4,5}
Arthur Kosowsky,^{4,5} Elena Pierpaoli,⁶ and Emmanuel Schaan^{7,8}

¹*Perimeter Institute for Theoretical Physics, 31 Caroline St N, Waterloo, ON N2L 2Y5, Canada*

²*Lawrence Berkeley National Laboratory, One Cyclotron Road, Berkeley, CA 94720, USA*

³*Berkeley Center for Cosmological Physics, Department of Physics, University of California, Berkeley, CA 94720, USA*

⁴*Department of Physics and Astronomy, University of Pittsburgh, 3941 O'Hara Street, Pittsburgh, PA 15260, USA*

⁵*Pittsburgh Particle Physics, Astrophysics, and Cosmology Center*

(PITT PACC), University of Pittsburgh, Pittsburgh, PA 15260, USA

⁶*Physics & Astronomy Department, University of Southern California, Los Angeles, California, 90089-0484*

⁷*Kavli Institute for Particle Astrophysics and Cosmology, 382 Via Pueblo Mall Stanford, CA 94305-4060, USA*

⁸*SLAC National Accelerator Laboratory, 2575 Sand Hill Road Menlo Park, California 94025, USA*

The moving lens effect is a secondary CMB anisotropy induced by the transverse motion of gravitational potentials. We develop a Fourier-space cross-spectrum estimator that retains the scale dependence of the signal, and apply it to the Atacama Cosmology Telescope (ACT) DR6 CMB temperature maps and luminous red galaxies from the DESI Legacy Imaging Surveys. Using the foreground-reduced ACT NILC map, we find strong evidence for a non-zero amplitude of the cross-correlation $b_{\text{ML}} = 1.24 \pm 0.26$ (4.8σ) for the extended sample and 0.93 ± 0.25 (3.7σ) for the main sample, both consistent with the halo-model prediction for the moving lens signal. Our Fourier-based pipeline enforces separation of scales between the reconstructed velocities and the cross-correlation, which we show is essential for foreground mitigation. The residual foreground contamination is expected to be significantly smaller than the signal from both simulations and the multi-frequency analysis presented in this paper. No curl-mode test exceeds 2σ , and the results are robust across analysis variants. They constitute the first detection of the moving lens effect and unlock access to transverse velocities, a new cosmological probe. When combined with the kinematic Sunyaev-Zel'dovich effect, this provides a path toward mapping the three-dimensional velocity field of the Universe, opening a new avenue for probing the growth of structure and gravity on large scales.

I. INTRODUCTION

Peculiar velocities of large-scale structure carry information about the growth rate of cosmic perturbations, the nature of gravity, and the initial conditions of the universe. The radial component of the velocity field — the projection along the line of sight — has been studied extensively through redshift-space distortions in galaxy surveys [1] and through the kinetic Sunyaev-Zel'dovich (kSZ) effect, which imprints a Doppler shift on CMB photons scattered by free electrons in motion [2–6]. The *transverse* component — perpendicular to the line of sight — has, by contrast, remained largely inaccessible to observation. Accessing both components of the velocity field would provide additional avenues for cosmological inference, from breaking the optical-depth degeneracy inherent in kSZ measurements to enable independent constraints on the growth rate $f\sigma_8$ and the amplitude of local primordial non-Gaussianity f_{NL} [7, 8].

The moving lens effect provides a path to measuring transverse velocities from the CMB. First discussed by Birkinshaw & Gull [9] in 1983 and studied further by Aghanim et al. [10], the effect arises because a gravitational potential well moving transverse to the line of sight produces a time-varying potential along the photon path. CMB photons traversing such a potential experience a net energy shift, also known as the integrated Sachs-Wolfe effect [11, 12], here sourced by bulk transverse motion rather than by the growth or decay of potentials. The resulting temperature anisotropy is proportional to the line-of-sight integral of $\nabla_{\perp}\Psi \cdot \mathbf{v}_{\perp}$ (Eq. 4), where Ψ is the Weyl potential and \mathbf{v}_{\perp} is the transverse peculiar velocity. For a single halo, the signal is a temperature *dipole* oriented along the direction of the halo's transverse motion, with an amplitude proportional to the lensing deflection angle times v_{\perp}/c . Two physically equivalent pictures describe the effect: in the CMB rest frame, it is a non-linear ISW contribution from the motion of potentials; in the rest frame of the lens, it is the gravitational lensing of the CMB kinematic dipole as seen by the moving halo [13].

A distinctive feature of the moving lens signal is that it is *purely gravitational*. Unlike the kSZ effect, which depends on the electron density, ionization fraction, and optical depth of intervening gas, the moving lens signal depends only

* shotinli@perimeterinstitute.ca

on the gravitational potential and the velocity field. This makes it insensitive to the baryonic physics that introduces an optical-depth degeneracy between the signal amplitude and the electron profile of halos in kSZ measurements [6]. The moving lens signal also has a blackbody frequency spectrum, identical to that of the primary CMB, which means it survives internal linear combination (ILC) cleaning but cannot be separated from the primary CMB, kSZ, or halo lensing signals by frequency information alone.

Several studies have developed the theoretical framework for detecting the moving lens effect. Hotinli et al. [13] introduced a quadratic estimator — analogous to standard CMB lensing reconstruction — that cross-correlates small-scale CMB temperature with a density-derived gravitational potential map to reconstruct the large-scale transverse velocity potential, forecasting detection at $\sim 8\sigma$ with the Simons Observatory [14] combined with DES and $\sim 40\sigma$ with CMB-S4 combined with LSST [15]. Hotinli, Johnson & Meyers [16] developed a complementary real-space matched-filter approach, deriving optimal filters for extracting transverse velocities from CMB cutouts around individual halos, and finding consistent signal-to-noise forecasts. Yasini, Mirzatumy & Pierpaoli [17] proposed a pairwise transverse-velocity estimator — the transverse analog of the pairwise kSZ statistic — as an additional detection pathway.

The cosmological science case for the moving lens was demonstrated by Hotinli et al. [8], who showed that transverse velocity reconstruction can measure $f\sigma_8$ to high precision by breaking two degeneracies that limit other probes: the optical-depth degeneracy in kSZ tomography (where $f\sigma_8$ is degenerate with the galaxy-electron cross-power spectrum P_{ge}), and the RSD bias in galaxy clustering (where tidal alignment effects introduce a multiplicative bias b_{rsd} on the inferred growth rate [18]). Like in the case of velocity reconstruction from kSZ, moving-lens tomography reconstructs velocities up to an overall bias b_{\perp} . This bias depends instead on the galaxy-gravitational-potential cross-power spectrum $P_{g\Psi}$, a quantity that can be calibrated with galaxy-lensing measurements, providing an independent and complementary constraint. Combined with kSZ and galaxy clustering in a joint analysis, moving lens tomography can improve constraints on $f\sigma_8$ substantially, particularly when astrophysical systematic uncertainties are large.

More recently, significant attention has been given to the practical challenges of extracting the moving lens signal from realistic CMB and galaxy data. Hotinli et al. [19] identified a previously unrecognized potential source of contamination: correlations between the gradients of extragalactic foreground emission (tSZ and CIB) and the transverse velocity field. Because halos tend to move toward overdense regions, the foreground emission is enhanced ahead of the halo in the direction of its transverse motion, producing a pattern morphologically similar to the moving lens signal, but up to an order of magnitude larger on single-frequency maps. This foreground signal has a different frequency dependence and spatial profile than the moving lens, offering potential routes to mitigation through multi-frequency component separation or through the scale-dependence of the signal.

Two independent groups have since performed realistic, map-based forecasts that incorporate correlated non-Gaussian foregrounds. Hotinli & Pierpaoli [20] used the WEBSKY simulation to evaluate both oriented stacking and pairwise estimation methods, finding that residual CIB, tSZ, and halo lensing gradients make the moving lens detection difficult, unless these foregrounds are well understood and/or mitigated. Beheshti, Schaan & Kosowsky [21] arrived at broadly consistent conclusions and introduced a template deprojection technique that partially removes the isotropic foreground signal correlated with galaxy positions while preserving the moving lens dipole. They forecast signal-to-noise ratios ranging from ~ 2 for ACT \times DESI Y1 to ~ 10 for SO \times DESI Y5 and ~ 100 for S4 \times LSST with optimal mass weighting, and emphasize that increasing galaxy number counts is more effective than improving CMB sensitivity for detection. These forecasts suggest that current Stage-3 data may be sensitive to the moving lens signal.

In this work, we present a new approach to measuring the moving lens signal. Rather than using the quadratic estimator formalism of [13] or stacking CMB patches at individual halo locations (the matched-filter approach), we construct a transverse velocity template from a galaxy density field [22, 23]. Our approach is similar in spirit to the matched-filter analysis of Ref. [16], but retains the scale dependence of the cross-spectrum rather than integrating over ℓ , which provides direct sensitivity to the scale dependence and frequency dependence of the signal. We cross-correlate the spin-1 gradient-mode harmonic coefficients with the CMB temperature in harmonic space to measure the angular power spectrum C_{ℓ}^{TG} . This spectrum is proportional to (and provides a direct measurement of) the galaxy-potential cross-power spectrum $P_{g\Psi}(k)$.

The harmonic-space framework provides a clean separation between signal and noise as a function of angular scale and connects directly to the theoretical prediction for C_{ℓ}^{TG} . The normalization is computed using surrogate Gaussian random fields [24], a technique that accounts for the survey geometry, selection function, and masks without requiring mock simulations. It also allows a clean separation of scales between the transverse-velocity template and the scales used in the analysis, which we will show is crucial for foreground mitigation.

We apply this estimator to CMB temperature maps from the Atacama Cosmology Telescope (ACT) [25, 26] cross-correlated with galaxy catalogs from the DESI Legacy Imaging Surveys [27, 28]. We fit each CMB map indepen-

dently and use the consistency of b_{ML} across frequencies, together with null tests from frequency-difference maps and curl-mode cross-spectra, to assess foreground contamination. As a conservative cross-check, we also inspect the cross-correlation of *Planck* 353 and 545 GHz maps [29] with the velocity template as a sensitive test of possible CIB contamination, and evaluate the expected foreground biases in a simulation pipeline based on Quijote N -body snapshots [30] and simplified tSZ/CIB models [31]. Applying this pipeline to ACT DR6 \times DESI LS yields the first observational detection of the moving lens effect at 4.8σ in the foreground-cleaned NILC map for the extended LRG sample (at 3.7σ in the main sample).

The remainder of this paper is organized as follows. Section II establishes notation, introduces the spin-1 gradient/curl decomposition of the vector fields on the sphere, and defines the moving lens signal. Section III describes the pipeline, including the $P_{g\Psi}$ estimator, surrogate-field normalization, and statistical analysis framework. Section IV describes the galaxy catalogs and CMB maps used. Section V presents the b_{ML} measurements from NILC and the single-frequency channels, null tests from frequency-difference and curl-mode cross-spectra, and robustness checks. Section VI bounds CIB contamination empirically using Planck 353 and 545 GHz cross-correlations, and evaluates foreground biases in a simulation pipeline based on Quijote N -body snapshots. Section VII discusses the implications and concludes. Technical details of the normalization and the simulation pipeline appear in Appendices A and C.

II. PRELIMINARIES

We denote three-dimensional comoving positions by \mathbf{x} and two-dimensional sky directions by $\boldsymbol{\theta}$ (a unit three-vector). The comoving distance to redshift z is $\chi(z)$; we will sometimes change variables $\chi \leftrightarrow z$ without comment. Our Fourier convention is

$$f(\mathbf{x}) = \int \frac{d^3\mathbf{k}}{(2\pi)^3} \tilde{f}(\mathbf{k}) e^{i\mathbf{k}\cdot\mathbf{x}}, \quad \tilde{f}(\mathbf{k}) = \int d^3\mathbf{x} f(\mathbf{x}) e^{-i\mathbf{k}\cdot\mathbf{x}}. \quad (1)$$

We use the shorthand integral notation (for a fixed 3-d vector \mathbf{K}):

$$\int_{\mathbf{k}+\mathbf{k}'=\mathbf{K}} (\dots) = \int \frac{d^3\mathbf{k}}{(2\pi)^3} \frac{d^3\mathbf{k}'}{(2\pi)^3} (\dots) (2\pi)^3 \delta^3(\mathbf{k} + \mathbf{k}' - \mathbf{K}). \quad (2)$$

We denote 3-d vector indices by i, j, \dots . In a 2-d spherical geometry, we denote tangent vector indices by $a, b, \dots \in \{\theta, \phi\}$. For example, a 2-d vector field would be denoted $X_a(\boldsymbol{\theta})$ in pixel space. In harmonic space, we use a gradient/curl representation ($X_{\ell m}^G, X_{\ell m}^C$) for vector fields:

$$(X_\theta \pm iX_\phi)(\boldsymbol{\theta}) = \sum_{\ell m} (\mp X_{\ell m}^G - i X_{\ell m}^C)_{\pm 1} Y_{\ell m}(\boldsymbol{\theta}). \quad (3)$$

The gradient coefficients $X_{\ell m}^G$ have parity $(-1)^\ell$ (electric type) and the curl coefficients $X_{\ell m}^C$ have parity $(-1)^{\ell+1}$ (magnetic type).

The moving lens contribution to the CMB temperature anisotropy is a line-of-sight integral coupling the transverse velocity field to the gradient of the gravitational potential [9, 10]:

$$\Theta_{\text{ML}}(\boldsymbol{\theta}) = -2T_{\text{CMB}} \int d\chi \nabla_\perp \Psi(\mathbf{x}) \cdot \mathbf{v}_\perp(\mathbf{x}), \quad (4)$$

where Ψ is the Weyl potential and \mathbf{v}_\perp is the velocity transverse to the line of sight.

III. PIPELINE DESCRIPTION

A. Intuitive idea and simplified pipeline

In this section, we construct a simplified version of our moving-lens estimator, in a flat-sky ‘‘snapshot’’ geometry with no survey mask or lightcone evolution, and build intuition by emphasizing similarity with kSZ estimators. In the next section (§III B), we relax these simplifying assumptions and construct an estimator that can be applied to real data.

In the snapshot geometry, large-scale structure fields are defined in a 3-d periodic box of side length L , at a fixed redshift z_* . The CMB is a 2-d flat-sky field obtained by projecting onto one periodic face of the box, and switching to angular coordinates $\boldsymbol{\theta} = (\mathbf{x}^\perp/\chi_*)$.

Review of kSZ Fourier-space estimator. Our moving lens estimator is very similar to estimators that measure the galaxy-electron power spectrum $P_{ge}(k)$ using the kSZ effect, especially the Fourier-space estimators from [32–34]. Roughly speaking, the moving lens estimator is the “kSZ estimator with more indices”: some scalar quantities become vector fields. We briefly review kSZ estimators, before constructing a moving-lens estimator.

Let $\delta_g(\mathbf{x})$ be a galaxy field with 3-d comoving number density n_g^{3d} , and let $\hat{v}_j(\mathbf{x})$ be a large-scale velocity reconstruction derived from δ_g . In this paper, we use a linear reconstruction:

$$\hat{v}_j(\mathbf{k}) = (ik_j)U(k)\delta_g(\mathbf{k}) \quad \text{where } U(k) \equiv \begin{cases} \frac{faH}{k^2b_g} \frac{P_{gg}(k)}{P_{gg}^{\text{tot}}(k)} & k < k_{\text{max}}, \\ 0 & \text{otherwise.} \end{cases} \quad (5)$$

where $P_{gg}^{\text{tot}}(k), P_{gg}(k)$ denote the galaxy power spectrum with and without Poisson noise. However, the precise form of the velocity reconstruction will not be very important. To quantify the fidelity of the reconstruction, we define parameters η_r, η_\perp by:

$$\langle v_r^{\text{true}}(\mathbf{x}) \hat{v}_r(\mathbf{x}) \rangle = \eta_r, \quad \langle v_a^{\text{true}}(\mathbf{x}) \hat{v}_b(\mathbf{x}) \rangle = \frac{\eta_\perp}{2} \delta_{ab}, \quad (6)$$

where v_r denotes the radial component of the velocity field¹, and $a, b \in \{1, 2\}$ denotes transverse components.

In the kSZ case, we construct a 2-d field $\pi(\boldsymbol{\theta})$ by summing galaxies weighted by radial velocities:

$$\pi(\boldsymbol{\theta}) = \sum_{i \in \text{gal}} \hat{v}_r(\mathbf{x}_i) \delta^2(\boldsymbol{\theta} - \boldsymbol{\theta}_i). \quad (7)$$

Then, it can be shown that the kSZ effect produces a correlation $C_l^{T\pi} \neq 0$ between the CMB temperature and the π -field:

$$C_l^{T\pi} = \eta_r n_g^{3d} K_* L P_{ge}(l/\chi_*) \quad \text{where } K_* \equiv -T_{\text{CMB}} \sigma_T n_{e0} (1 + z_*)^2. \quad (8)$$

We omit the derivation of Eq. (8), since we do the analogous calculation for the moving-lens effect in detail below. Thus, the estimator $C_l^{T\pi}$ can be used to detect the kSZ effect, and measure $P_{ge}(k)$ as a function of k .

Moving-lens estimator. How should the preceding construction be modified for the moving lens effect? Intuitively, instead of weighting galaxies by radial velocities (as in Eq. (7)), we want to weight them by transverse velocities. Thus, we get a vector (spin-one) field $X_a(\boldsymbol{\theta})$, instead of a scalar (spin-zero) field $\pi(\boldsymbol{\theta})$:

$$X_a(\boldsymbol{\theta}) = \sum_{i \in \text{gal}} \hat{v}_a(\mathbf{x}_i) \delta^2(\boldsymbol{\theta} - \boldsymbol{\theta}_i). \quad (9)$$

We decompose X_a into its gradient and curl modes X_G, X_C . This step is the flat-sky analog of Eq. (3), and is naturally written in Fourier space:

$$X_a(\mathbf{l}) = \frac{i l_a}{l} G(\mathbf{l}) + \frac{i \epsilon_{abl} b_b}{l} C(\mathbf{l}). \quad (10)$$

We claim that the moving lens effect produces a correlation $C_l^{TG} \neq 0$ between the CMB temperature and the **gradient mode of the X-field**. The rest of this subsection is devoted to deriving this result.

¹ In the kSZ literature, a quantity closely related to η_r is typically used to normalize the estimators, that is, the correlation coefficient between true and reconstructed radial velocities $r_v \equiv \eta_r / [\sigma(v_r^{\text{true}}) \sigma(\hat{v}_r)]$.

First, we write $T_{ML}(\boldsymbol{\theta})$ and $X_a(\boldsymbol{\theta})$ (Eqs. (4), (9)) in flat-sky Fourier space:

$$T_{ML}(\mathbf{l}) = -2 \frac{T_{\text{CMB}}}{\chi_*^2} \int_{\mathbf{k}_L + \mathbf{k}_S = \mathbf{l}/\chi_*} v_b^{\text{true}}(\mathbf{k}_L) (\partial_b \Psi(\mathbf{k}_S)), \quad (11)$$

$$X_a(\mathbf{l}) = n_g^{3d} \int_{\mathbf{k}_L + \mathbf{k}_S = \mathbf{l}/\chi_*} \hat{v}_a(\mathbf{k}_L) \delta_g(\mathbf{k}_S). \quad (12)$$

Using these expressions, we compute the two-point function $\langle TX_a \rangle$, using a sequence of ‘‘squeezed’’ approximations which are familiar from the kSZ context:

$$\begin{aligned} \langle T_{ML}(\mathbf{l}) X_a(\mathbf{l}') \rangle &\sim \left(v_b^{\text{true}}(\partial_b \Psi) \right) \left(\hat{v}_a \delta_g \right) && \text{(schematic)} \\ &= -2 \frac{n_g^{3d} T_{\text{CMB}}}{\chi_*^2} \int_{\substack{\mathbf{k}_L + \mathbf{k}_S = \mathbf{l}/\chi_* \\ \mathbf{k}'_L + \mathbf{k}'_S = \mathbf{l}'/\chi_*}} \langle v_b^{\text{true}}(\mathbf{k}_L) \hat{v}_a(\mathbf{k}'_L) \rangle (i\mathbf{k}_S)_b \langle \Psi(\mathbf{k}_S) \delta_g(\mathbf{k}'_S) \rangle \\ &\approx -2 \frac{n_g^{3d} T_{\text{CMB}}}{\chi_*^2} \left(\frac{\eta_\perp}{2} \delta_{ab} \right) \left(\frac{i\mathbf{l}_b}{\chi_*} \right) P_{g\Psi} \left(\frac{\mathbf{l}}{\chi_*} \right) L \chi_*^2 (2\pi)^2 \delta^2(\mathbf{l} + \mathbf{l}') \\ &= \mathcal{N} (i\mathbf{l}'_a) P_{g\Psi} \left(\frac{\mathbf{l}}{\chi_*} \right) (2\pi)^2 \delta^2(\mathbf{l} + \mathbf{l}') && \text{where } \mathcal{N} \equiv \frac{\eta_\perp n_g^{3d} T_{\text{CMB}} L}{\chi_*}. \end{aligned} \quad (13)$$

In the first line, we made the approximation that the velocity reconstruction only has fluctuations on scales $k_L \ll (l/\chi_*)$, so that the four-point function on the RHS is well-approximated by the indicated Wick contraction. In the second and third lines, we evaluated the Wick contraction explicitly in the approximation $\mathbf{k}_S \approx (\mathbf{l}/\chi_*)$. From this calculation, we can read off the power spectra in the gradient/curl basis:

$$C_\ell^{TG} = \mathcal{N} \ell P_{g\Psi}(\ell/\chi_*), \quad C_\ell^{TC} = 0. \quad (14)$$

Note that $C_\ell^{TC} = 0$ can also be seen directly from symmetry, since the moving-lens effect is parity-symmetric.

This concludes our derivation that the moving lens effect produces a correlation $C_\ell^{TG} \neq 0$ with the gradient mode of the X -field, as claimed above. The correlation is proportional to $P_{g\Psi}(\ell/\chi_*)$, and the normalization \mathcal{N} is given by Eq. (13). Analogously to the kSZ case, the estimator C_ℓ^{TG} can be used to detect the moving-lens effect and to measure $P_{g\Psi}(k)$ as a function of k .

The galaxy–potential cross-power spectrum $P_{g\Psi}(k)$ is related to the galaxy–matter power spectrum $P_{gm}(k)$ via the Poisson equation:

$$P_{g\Psi}(k, z) = -\frac{3 H_0^2 \Omega_{m0}}{2 a k^2} P_{gm}(k, z). \quad (15)$$

Since $P_{gm}(k) > 0$, both $P_{g\Psi}(k)$ and C_ℓ^{TG} are negative.

We compute a fiducial galaxy–matter power spectrum $P_{gm}^{\text{fid}}(k)$ using the HMVEC halo-model code [6, 35], at the effective redshift $z_* = 0.734$. We use the default HMVEC HOD, abundance-matched to the 3-d number density of the DESI-LS galaxies. This results in a slightly different $P_{gm}^{\text{fid}}(k)$ for the main and extended DESILS LRG samples (see §IV A). The resulting predictions for DESI-LS quantities such as the mean halo bias agree at the $\sim 10\%$ level. The shape of $P_{g\Psi}(k)$ is well-constrained by this procedure; the absolute amplitude carries somewhat larger modeling uncertainty since it’s proportional to the mean halo mass, rather than the bias. In future work, it can be calibrated externally with galaxy or CMB lensing measurements [36].

B. Curved-sky pipeline and surrogate normalization

In this subsection, we describe our pipeline for detecting the moving lens effect in ACT and DESILS. The intuitive idea is the same as our simplified pipeline in §III A, but we now incorporate the complications of real data: an angular mask, redshift evolution, curved-sky geometry. Many of the details follow our previous paper [24], which constructed kSZ (radial velocity) estimators for the same datasets (ACT and DESILS-LRG).

We surround the 3-d DESILS footprint with a periodic bounding box, padded to mitigate artifacts from periodic

boundary conditions. Three-dimensional fields are represented in Cartesian coordinates in the bounding box, or in harmonic space via 3-d FFTs. Two-dimensional fields are represented as curved-sky `pixell` maps, or in harmonic space via spherical transforms.

First, we define the weighted galaxy overdensity $\rho_g(\mathbf{x})$ by the standard galaxies-minus-randoms prescription:

$$\rho_g(\mathbf{x}) = \sum_{i \in \text{gal}} W_i \delta^3(\mathbf{x} - \mathbf{x}_i) - \frac{N_g}{N_r} \sum_{j \in \text{rand}} W_j \delta^3(\mathbf{x} - \mathbf{x}_j), \quad (16)$$

where W_i is a per-object weight, and $N_g = \sum_i W_i$, $N_r = \sum_j W_j$ are the weighted galaxy and random counts. This definition of $\rho_g(\mathbf{x})$ accounts for the survey geometry (via the random catalog), and includes a per-object weight W_i to encode completeness, FKP weighting, and other complications. In our DESILS pipeline, we choose W_i to downweight galaxies with large photo- z errors (see Eq. (27) below).

Second, we compute the velocity reconstruction $\hat{v}_j(\mathbf{x})$ via a linear filtering operation similar to Eq. (5), but using the galaxy density ρ_g defined above:

$$\hat{v}_j(\mathbf{x}) = \int \frac{d^3\mathbf{k}}{(2\pi)^3} (ik_j) U(k) e^{i\mathbf{k}\cdot\mathbf{x}} \rho_g(\mathbf{k}) \quad \text{where } U(k) \equiv \begin{cases} \frac{faH}{k^2 b_g} \frac{P_{gg}(k)}{P_{gg}^{\text{tot}}(k)}, & k < k_{\text{max}}, \\ 0, & \text{otherwise.} \end{cases} \quad (17)$$

Here, f is the linear growth rate, a the scale factor, H the Hubble parameter, b_g the linear galaxy bias, and $P_{gg}^{\text{tot}} = P_{gg} + 1/\bar{n}_g^{3d}$ includes shot noise. The prefactor $ik_j faH/(k^2 b_g)$ converts the galaxy density contrast to a velocity via the continuity equation, while $P_{gg}/P_{gg}^{\text{tot}}$ is a Wiener filter that suppresses noise-dominated modes. All redshift-dependent quantities in Eq. (17), such as f, b_g, \bar{n}_g^{3d} , are evaluated at the central redshift $z_* = 0.734$ of DESILS.

Third, we compute a moving-lens template field $X_a(\boldsymbol{\theta})$ by:

$$X_a(\boldsymbol{\theta}) = \sum_{i \in \text{gal}} W_i \hat{v}_a(\mathbf{x}_i) \delta^2(\boldsymbol{\theta} - \boldsymbol{\theta}_i) - \frac{N_g}{N_r} \sum_{j \in \text{rand}} W_j \hat{v}_a(\mathbf{x}_j) \delta^2(\boldsymbol{\theta} - \boldsymbol{\theta}_j), \quad (18)$$

where the notation \hat{v}_a (as opposed to \hat{v}_j) means that we project onto the transverse (to \mathbf{x}) directions $a \in \{\theta, \phi\}$ (see §II). The definition of $X_a(\boldsymbol{\theta})$ is similar to Eq. (9) in our simplified pipeline, but we include a per-galaxy weight W_i (see above), and $X_a(\boldsymbol{\theta})$ is now a curved-sky 2-d field.

When we decompose $X_a(\boldsymbol{\theta})$ into gradient/curl components $X_{\ell m}^G, X_{\ell m}^C$, we use the curved-sky decomposition in Eq. (3). We then compute:

$$C_\ell^{TG} = \frac{1}{2\ell + 1} \sum_m X_{\ell m}^G T_{\ell m}^*, \quad (19)$$

with no f_{sky} correction on the RHS (that is, C_ℓ^{TG} always denotes a ‘‘pseudo’’ power spectrum in this paper). As in our simplified pipeline, the statistic C_ℓ^{TG} can be used to detect the moving lens effect, or to measure the power spectrum $P_{g\Psi}(k)$.

However, in our full (non-simplified) pipeline, the relation between C_ℓ^{TG} and $P_{g\Psi}(k)$ turns out to be more complicated. In Appendix A, we’ll show that:

$$C_\ell^{TG} = \mathcal{N} \ell b_\ell P_{g\Psi}(\ell/\chi_*) \quad \text{where } \mathcal{N} \equiv \frac{T_{\text{CMB}}}{4\pi} \sum_{j \in \text{gal}} W_j \frac{\eta_\perp(\mathbf{x}_j)}{\chi_j^3}. \quad (20)$$

where a CMB beam b_ℓ has been included, and the 3-d field $\eta_\perp(\mathbf{x})$ is defined by:

$$\eta_\perp(\mathbf{x}) \equiv \left\langle \sum_{a \in \{\theta, \phi\}} \hat{v}_a(\mathbf{x}) v_a^{\text{true}}(\mathbf{x}) \right\rangle. \quad (21)$$

Note that $\eta_\perp(\mathbf{x})$ is a 3-d field that depends on both redshift (due to evolution) and angular location (due to boundary effects from the survey mask). This definition of $\eta_\perp(\mathbf{x})$ generalizes the scalar quantity η_\perp in the simplified pipeline (Eq. (6)).

The relation (20) between C_ℓ^{TG} and $P_{g\Psi}(k)$ is nontrivial to derive, and we defer the details to Appendix A. In this appendix, we also show how to compute $\eta_\perp(\mathbf{x})$ and \mathcal{N} using a Monte Carlo procedure (“surrogate fields”). The technical challenge of computing \mathcal{N} is somewhat tangential for purposes of this paper, since \mathcal{N} is not needed for assessing detection significance, null test failure, or the “shape” in ℓ of the fiducial moving-lens signal. The value of \mathcal{N} is only needed to compare the amplitude of $P_{g\Psi}(k)$ to a fiducial model. (Note that the amplitude has large modeling uncertainty – see the discussion at the end of §III A.)

C. Statistical analysis

After estimating C_ℓ^{TG} , we bin the power spectrum in ℓ , obtaining a “data vector” d_b , where $1 \leq b \leq N_b$ indexes an ℓ -bin. We use the following binning procedure:

$$d_b = \frac{1}{W_b} \sum_{\ell \in b} w_\ell D_\ell, \quad (22)$$

where $D_\ell \equiv \ell^2 C_\ell^{TG}$, and the ℓ -weighting within a bin is $w_\ell \equiv (2\ell + 1)$, and $W_b \equiv \sum_{\ell \in b} w_\ell$. We use $N_b = 6$ logarithmically-spaced bins spanning $\ell \in [2500, 6000]$.

We estimate the covariance $C_{bb'} = \text{Cov}(d_b, d_{b'})$ from the scatter in D_ℓ between different values of ℓ . A slight complication is that on the partial sky, mode coupling correlates nearby multipoles over a range $\Delta\ell \sim 1/f_{\text{sky}}$. This motivates the following “empirical” estimate of the covariance matrix:

$$C_{bb'} = \frac{1}{W_b W_{b'}} \sum_{\substack{\ell \in b, \ell' \in b' \\ |\ell - \ell'| \leq \Delta\ell}} w_\ell w_{\ell'} D_\ell D_{\ell'}. \quad (23)$$

This is an unbiased estimator of $\text{Cov}(d_b, d_{b'})$, under the assumptions that $\text{Cov}(D_\ell, D_{\ell'}) = 0$ for $|\ell - \ell'| > (\Delta\ell)$, and that $\langle D_\ell \rangle = 0$ (as appropriate for the null hypothesis of no moving-lens detection). Note that off-diagonal correlations are either zero (if $|b - b'| > 1$) or very small (if $|b - b'| = 1$). For the DESI-LS LRG footprints, $f_{\text{sky}} \approx 0.09$ (NGC) and 0.19 (SGC), giving $\Delta\ell = 11$ and 5, respectively.

As a check on the empirical estimator (23) for the power spectrum covariance, we also implemented a different method based on simulations. We find that agreement between the two methods is excellent. The simulation-based method is described in Appendix B.

Throughout the paper, we quantify the moving-lens detection significance by fitting the data vector d_b to an overall multiple (denoted b_{ML}) of a moving lens template t_b . To obtain t_b , we start with the fiducial $P_{g\Psi}^{\text{fid}}(k)$ described at the end of §III A, convert to $C_\ell^{TG} = \mathcal{N} \ell b_\ell P_{g\Psi}(\ell/\chi_*)$, and bin in ℓ using Eq. (22). The likelihood function for b_{ML} is given by:

$$\ln \mathcal{L}(b_{\text{ML}}) = -\frac{1}{2} (\mathbf{d} - b_{\text{ML}} \mathbf{t})^T \mathbf{C}^{-1} (\mathbf{d} - b_{\text{ML}} \mathbf{t}). \quad (24)$$

Maximizing the Gaussian likelihood, we find that the best-fit b_{ML} value and its variance are given by:

$$\hat{b}_{\text{ML}} = \frac{\mathbf{t}^T \mathbf{C}^{-1} \mathbf{d}}{\mathbf{t}^T \mathbf{C}^{-1} \mathbf{t}}, \quad \sigma^2(b_{\text{ML}}) = \frac{1}{\mathbf{t}^T \mathbf{C}^{-1} \mathbf{t}}. \quad (25)$$

We use Eq. (25) throughout and quote \hat{b}_{ML} and σ as the best-fit value and uncertainty, respectively. When we analyze the NGC+SGC jointly, we add the log-likelihoods (assuming statistical independence). Note that the NGC and SGC have the same fiducial $P_{g\Psi}(k)$, but different fiducial $C_\ell^{TG} = \mathcal{N} \ell b_\ell P_{g\Psi}(\ell/\chi_*)$, since the normalization \mathcal{N} is different in the NGC and SGC (roughly as $\mathcal{N} \propto f_{\text{sky}}$).

To quote detection significance, we define the matched-filter signal-to-noise ratio:

$$\text{SNR} = \frac{\hat{b}_{\text{ML}}}{\sigma(b_{\text{ML}})} = \frac{\mathbf{t}^T \mathbf{C}^{-1} \mathbf{d}}{\sqrt{\mathbf{t}^T \mathbf{C}^{-1} \mathbf{t}}}, \quad (26)$$

D. Biases from CMB lensing, kSZ, and foregrounds

One might worry that ordinary (non-moving) CMB lensing would be a large contaminant to the moving-lens signal. However, there is a symmetry argument which shows that the lensing bias to C_ℓ^{TG} vanishes. Consider a symmetry which reverses the sign of the primary CMB temperature $T_{\text{pri}} \rightarrow (-T_{\text{pri}})$ on the last scattering surface, leaving large-scale structure in the late universe unmodified. The CMB lensing contribution to our moving-lens estimator C_ℓ^{TG} is odd under this symmetry. Therefore, the mean bias $\langle C_\ell^{TG} \rangle$ due to CMB lensing must be zero.

Going beyond mean bias, one may wonder whether statistical errors on C_ℓ^{TG} are affected by the non-Gaussian statistics of CMB lensing. Here, we note that the estimator C_ℓ^{TG} involves one power of CMB temperature, so its covariance $\text{Cov}(C_\ell^{TG}, C_{\ell'}^{TG})$ depends only on the two-point function C_ℓ^{TT} , not on higher-point statistics. Therefore, the effect of CMB lensing is no different from other contributions to the temperature power spectrum, and is fully captured by our method (§III C) for assigning error bars.

Similarly, one might worry that kSZ is a potential contaminant. Here, a different symmetry applies: radial reflection $v_r \rightarrow (-v_r)$ in the line-of-sight direction. (Note that this is an exact symmetry in the Limber/snapshot approximation, but an approximate symmetry in an evolving lightcone geometry.) The kSZ contribution to C_ℓ^{TG} is odd under this symmetry, so the same arguments as in the CMB lensing case apply, to show that kSZ contamination is not an issue.

Astrophysical foregrounds (tSZ, CIB, radio sources) are a different story: here there is no symmetry in sight, and foreground bias to the moving-lens estimator is a concern. Indeed, several previous studies [19–21] have found significant foreground biases to the moving-lens signal, and highlighted their importance. For this reason, our results and null tests in subsequent sections (§V, §VI) are largely aimed at quantifying foreground biases.

One of the main results of this paper is that CMB foreground biases to the moving-lens estimator are small, provided that the estimator is constructed in a particular way (Fourier-space throughout, hard k_{max} cutoff in the velocity reconstruction). We'll show this in two ways: either via frequency-difference null tests applied to data (§V C, §VIA), or via a simplified moving-lens pipeline applied to Quijote simulations (§VIB).

IV. DATA

We use the same galaxy catalog and CMB maps as in the kSZ analysis in Ref. [24]. This section summarizes the key properties of each data set and the preprocessing steps specific to the moving lens analysis.

A. Galaxy catalog

For the galaxy survey, we use the luminous red galaxy (LRG) sample from the DESI Legacy Imaging Surveys Data Release 9 (DESI-LS DR9) [28, 37, 38]. The DESI Legacy Imaging Surveys combine data from three optical programs — DECaLS, BASS, and MzLS — covering approximately 14 000 deg² of extragalactic sky [37]. The ‘main’ LRG target selection of Ref. [38] applies the strictest color and magnitude cuts, providing the most uniform photometry and the highest photometric redshift purity.

We apply the veto masks and quality cuts described in Ref. [39] (see also Section 3.3 of Ref. [38]). We analyze both the northern Galactic cap (NGC) and southern Galactic cap (SGC), as well as their combination. We further restrict to the photometric redshift range $0.4 \leq z_{\text{obs}} \leq 1.0$.

After all cuts and after restricting to sky regions where the CMB pixel weight $W_{\text{CMB}}(\boldsymbol{\theta}) > 0$ (see Section IV B below), the main LRG catalog contains 1,672,848 galaxies in NGC ($f_{\text{sky}} \approx 0.09$, effective area $\approx 3,670$ deg²), 3,410,551 in SGC ($f_{\text{sky}} \approx 0.19$, $\approx 7,710$ deg²). The NGC+SGC combination is performed at the bandpower level using inverse-variance weighting of independent per-cap fits (Section III C). The corresponding random catalogs we use contain 29,610,244 (NGC) and 61,888,997 (SGC) objects.

a. Extended sample. Throughout our figures, we display results from the extended sample with the ‘extended’ DESI-LS DR9 LRG target selection [38], which relaxes the color and magnitude cuts, providing a higher number density at the cost of slightly larger photometric redshift errors. The extended catalog contains 4,349,228 (NGC), 8,839,449 (SGC) galaxies over the same footprint as the main sample (the random catalogs are identical). Main and extended share the same sky coverage, with the extended sample adding fainter galaxies; the two are therefore not independent, and the two results serve as a consistency check rather than independent datasets.

b. Photometric redshifts. The main LRG sample has photometric redshift errors at the 2–3% level (normalized median absolute deviation NMAD ≈ 0.02 – 0.03), with an outlier fraction below 0.5% [28, 38].

The per-galaxy weights W_i that appear in the density field (Eq. 16) and in the velocity template (Eq. 18) are set to

$$W_i = \exp\left[-\frac{\sigma_{z,i}^2}{\alpha(1+z_i)^2}\right], \quad \alpha = 2.5 \times 10^{-3}, \quad (27)$$

where $\sigma_{z,i}$ is the photometric redshift error of galaxy i . This choice down-weights objects whose photo- z errors are large compared to the correlation length of the velocity field.

c. Random catalog. For the random catalog, we assign photometric redshifts by deconvolving the joint $(z_{\text{obs}}, \sigma_z)$ distribution of the galaxy sample, following the procedure described in Ref. [24]. Each random object is assigned a $(z_{\text{obs}}, z_{\text{true}}, \sigma_z)$ drawn from the inferred three-dimensional distribution, and the same redshift and quality cuts are applied. The random catalog is used both in the density field construction (Eq. 16) and in the surrogate normalization (Appendix A).

These are the same samples used in kSZ measurements of stacked gas profiles [40], as well as used for radial velocity reconstruction [24], thus allowing joint kSZ and ML analyses in the future.

B. CMB maps

We use the component-separated NILC temperature map from ACT Data Release 6 (DR6) [26], which combines ACT (DR4 and DR6, 93–225 GHz) and Planck NPIPE [29] (30–545 GHz) data to produce a minimum-variance CMB map over approximately 13,000 deg². The map is convolved to a common Gaussian beam with FWHM = 1.6' and has a mean white noise depth of approximately 15 $\mu\text{K-arcmin}$.

We also use single-frequency ACT DR6 co-added, source-free temperature maps [41] at central frequencies of 98 GHz, 150 GHz, and 220 GHz. The 98 GHz channel is referred to as “90 GHz” throughout, following the convention of the ACT data products. We use the night-only co-adds, which have reduced beam systematics on small scales. As a robustness check, we also repeat the analysis using the **daynight** co-adds, which combine daytime and nighttime observations and have somewhat smaller noise (Section V D).

a. Masking and pixel weights. We apply two layers of masking. First, we apply the Planck GAL070 galactic foreground mask, which retains 70% of the sky. Second, we define the CMB pixel weight as

$$W_{\text{CMB}}(\boldsymbol{\theta}) = \begin{cases} 1, & \text{if the noise in pixel } \boldsymbol{\theta} \text{ is } \leq 70 \mu\text{K-arcmin for both 90 and 150 GHz,} \\ 0, & \text{otherwise.} \end{cases} \quad (28)$$

The noise threshold is applied independently at each frequency, and we take the intersection so that both channels share the same sky footprint. No tSZ cluster mask is applied; we have verified that including one does not change our results.

b. Beam equalization. We match the effective beams of the 150 and 220 GHz maps to that of the 90 GHz channel by multiplying in harmonic space:

$$T_{\ell m}^\nu|_{b_{90}} = T_{\ell m}^\nu \frac{b_\ell^{90}}{b_\ell^\nu}, \quad (29)$$

where b_ℓ^ν denotes the beam transfer function at frequency ν . After this operation, all single-frequency channels share the same effective beam b_ℓ^{90} , which is the beam that appears in the theory prediction (Eq. 20); for NILC, the corresponding beam is b_ℓ^N (defined below).

c. Frequency differences. From the beam-equalized single-frequency maps, we construct three frequency-difference maps for use as null tests:

- *150–90 difference:* $T_{\ell m}^{150-90} = T_{\ell m}^{150}|_{b_{90}} - T_{\ell m}^{90}$, which cancels signals with a blackbody spectrum and serves as a null test for frequency-dependent systematics.
- *220–150 difference:* $T_{\ell m}^{220-150} = T_{\ell m}^{220}|_{b_{90}} - T_{\ell m}^{150}|_{b_{90}}$.
- *220–90 difference:* $T_{\ell m}^{220-90} = T_{\ell m}^{220}|_{b_{90}} - T_{\ell m}^{90}$.

d. 220 GHz noise mask. As a robustness check, we define a stricter masking condition that additionally requires the 220 GHz white-noise level to be below 300 $\mu\text{K-arcmin}$ in each pixel. This mask excludes the noisiest 220 GHz

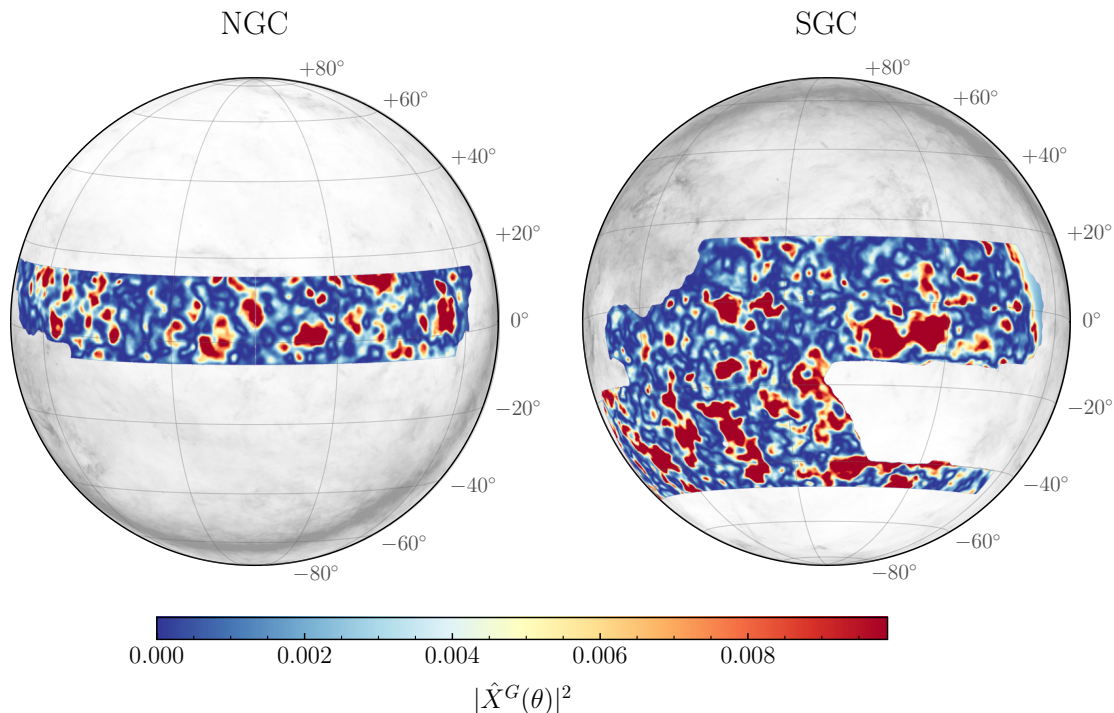


FIG. 1. Orthographic projection of $|X^G(\hat{n})|^2$ for the DESI-LS main LRG \times ACT DR6 dataset (random-subtracted). Left: NGC. Right: SGC. The colored region shows $|X^G(\hat{n})|^2$ at full opacity within the survey footprint (DESI-LS \cap ACT noise mask); the grayscale background shows the Planck 353 GHz GNILC thermal dust emission [42] at reduced opacity. $X^G(\hat{n})$ is the inverse SHT of $X_{\ell m}^G$ truncated at $\ell_{\max} = 2000$ and smoothed with a $50'$ FWHM Gaussian beam; the monopole and dipole have been removed within the footprint before squaring. RA/Dec coordinate lines are overlaid at 40° and 20° intervals, respectively.

regions and slightly reduces the effective sky footprint. All maps and galaxy catalogs are re-processed with this mask applied; the results are described in Section V D.

We compute cross-spectra $C_\ell^{TG} = \langle X_{\ell m}^G T_{\ell m}^* \rangle / (2\ell + 1)$ for each CMB map (NILC, single-frequency, and frequency-difference).

V. RESULTS

A. Velocity reconstruction

We apply the pipeline of Section III to the data described in Section IV. The galaxy density field $\rho_g(\mathbf{x})$ (Eq. 16) is computed on a three-dimensional grid with pixel size 10 Mpc and a bounding-box padding of 3000 Mpc to suppress periodic boundary artifacts. The Wiener filter (Eq. 17) is applied with a cutoff $k_{\max} = 0.05 \text{ Mpc}^{-1}$ and a fiducial galaxy bias $b_g = 2.054$.

The resulting transverse velocity components $\hat{v}_\theta(\mathbf{x})$ and $\hat{v}_\phi(\mathbf{x})$ are evaluated at each galaxy position and painted onto HEALPix maps at $N_{\text{side}} = 4096$.² We construct two sets of maps: *galaxy-only* maps, which use only the galaxy sum in Eq. (18), and *random-subtracted* maps, which include the $(N_g/N_r) \sum_\beta$ random-catalog term from Eq. (16). The random subtraction removes the imprint of the survey selection function while preserving the correlated velocity signal.

Figure 1 shows $|X^G(\hat{n})|^2$, the squared real-space gradient mode of the random-subtracted velocity field, in orthographic projection centered on the northern (NGC, left) and southern (SGC, right) Galactic caps. We obtain $X^G(\hat{n})$ as the inverse spherical-harmonic transform of $X_{\ell m}^G$ truncated at $\ell_{\max} = 2000$ and smoothed with a $50'$ FWHM Gaussian

² We reconstruct velocities on HEALPix maps and compute alms via healpy. We keep the CMB maps in their pixel CAR pixelization and compute alms via pixell.curvedsky. We reproject the Planck galactic-plane mask from galactic onto the pixel CAR grid before multiplying it with the CMB maps; both HEALPix and pixell maps are in equatorial coordinates.

beam; the monopole and dipole are removed within the survey footprint before squaring. The colored region shows the survey footprint ($\text{DESI-LS} \cap \text{ACT noise mask}$); the grayscale background shows the Planck 353 GHz GNILC dust emission [42] in the complementary sky area.

B. Signal measurements

We begin with the foreground-cleaned NILC map, which provides the lowest-noise constraints on b_{ML} . The NILC map minimizes the total power of foregrounds and noise using all available frequency channels [26], making it the minimum-variance choice for signals with a blackbody frequency dependence, such as the ML effect.

a. NILC beam. The NILC map is reconvolved to a Gaussian beam b_ℓ^N with FWHM = $1.6'$. Rather than correcting the data to b_ℓ^{90} , we convolve the theory template (Eq. 20) with b_ℓ^N directly when fitting the NILC bandpowers.

For the combined NGC+SGC footprint, the extended sample yields

$$b_{\text{ML}} = 1.24 \pm 0.26 \quad (4.8\sigma), \quad (30)$$

consistent with the fiducial halo-model prediction. The main sample gives $b_{\text{ML}} = 0.93 \pm 0.25$ (3.7σ).

We also fit b_{ML} independently to each single-frequency map (90, 150, and 220 GHz). For the extended sample (NGC+SGC) we find:

- 90 GHz: $b_{\text{ML}} = 0.93 \pm 0.36$ (2.6σ , $\chi^2/\text{dof} = 0.96$, $\text{PTE}(\text{gof}) = 0.44$),
- 150 GHz: $b_{\text{ML}} = 1.14 \pm 0.32$ (3.6σ , $\chi^2/\text{dof} = 0.47$, $\text{PTE}(\text{gof}) = 0.80$),
- 220 GHz: $b_{\text{ML}} = 3.08 \pm 1.29$ (2.4σ , $\chi^2/\text{dof} = 0.47$, $\text{PTE}(\text{gof}) = 0.80$).

where we also report the χ^2 of the one-parameter b_{ML} -fit, and the associated “goodness of fit” p -value, denoted $\text{PTE}(\text{gof})$. The main sample gives consistent amplitudes for 90 and 150 GHz: $b_{\text{ML}} = 0.74 \pm 0.35$ (90 GHz), 0.62 ± 0.31 (150 GHz); whereas for 220 GHz, $b_{\text{ML}} = 2.92 \pm 1.28$. Table I collects the full set of results for both samples and all footprints.

Figure 2 shows the gradient-mode bandpowers for all four CMB maps (NILC, 90, 150, and 220 GHz) and all three footprints (NGC+SGC, NGC, SGC) for the extended sample. The NILC results (first row) follow the ML template across the full multipole range. The NILC map, which minimizes the combined foreground and noise power across all channels, recovers an amplitude consistent with unity ($b_{\text{ML}} = 1.24 \pm 0.26$).

b. Sub-region (NGC vs SGC) analysis. For the extended sample, the NGC and SGC sub-regions yield $b_{\text{ML}} = 1.18 \pm 0.33$ (3.6σ) and 1.33 ± 0.42 (3.2σ), respectively. The main sample shows consistent amplitudes across sub-regions: $b_{\text{ML}} = 0.94 \pm 0.36$ (NGC) and 0.93 ± 0.36 (SGC).

The individual-frequency bandpowers are shown alongside the NILC results in Figure 2 (rows 2–4). At 150 GHz (third row), the bandpowers have a high goodness of fit ($\text{PTE}(\text{gof}) = 0.80$); the NGC and SGC amplitudes are 1.19 ± 0.43 and 1.07 ± 0.48 , both consistent with unity. At 220 GHz (fourth row), the larger scatter reflects the higher noise level, but the template shape remains an acceptable fit. The NGC and SGC amplitudes are consistent across samples (extended 3.47 ± 1.60 NGC vs 2.32 ± 2.21 SGC, while for the main, 3.66 ± 1.89 NGC vs 2.29 ± 1.74 SGC).

C. Null tests

We perform three classes of null tests: curl mode, frequency differences, and NGC-SGC consistency, described below. All null tests are collected in Table II.

a. Curl mode. As shown in Eq. (14), the curl-mode correlation C_ℓ^{TC} vanishes by parity symmetry; non-zero power would indicate parity-asymmetric systematics. The curl-mode cross-spectra for all four CMB maps are shown in Figure 3. For the extended sample (NGC+SGC), all four channels yield b_{ML} consistent with zero at low significance: NILC (0.5σ , $p_0 = 0.65$), 90 GHz (0.8σ , $p_0 = 0.43$), 150 GHz (1.0σ , $p_0 = 0.31$), and 220 GHz (0.1σ , $p_0 = 0.91$). The χ^2/dof values range from 0.13 to 1.60, with goodness-of-fit probabilities in [0.16, 0.98] – all above 0.05. The NGC and SGC sub-regions are individually consistent with zero for all channels (Table II).

For the main sample (NGC+SGC), the curl-mode amplitudes are again consistent with zero: NILC (0.5σ , $p_0 = 0.58$), 90 GHz (1.2σ , $p_0 = 0.24$), 150 GHz (0.1σ , $p_0 = 0.95$), and 220 GHz (0.6σ , $p_0 = 0.52$). No curl-mode test reaches 2σ significance for either sample.

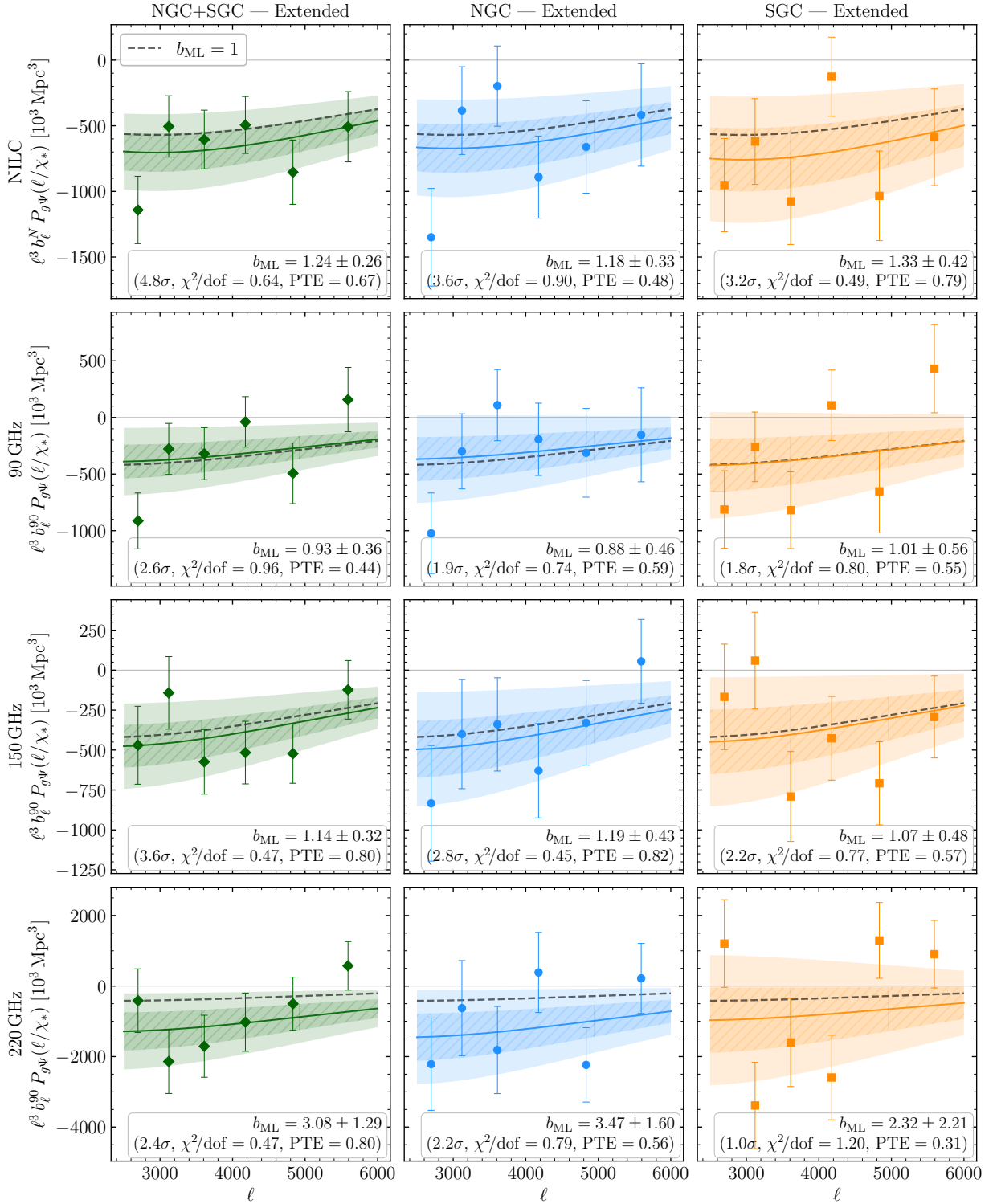


FIG. 2. The NILC and 90, 150 and 220 GHz bandpowers for the DESI-LS extended LRG sample. Panels show the gradient mode $X_{\ell m}^G$. From left to right: NGC+SGC (inverse-variance weighted), NGC, SGC. Solid curves: best-fit b_{ML} template; darker hatched bands: 1σ ; lighter smooth bands: 2σ . Dashed curve corresponds to $b_{\text{ML}} = 1$.

b. Frequency differences. Frequency-difference maps cancel any signal with a blackbody spectrum, so a non-zero amplitude in 150–90, 220–90, or 220–150 would indicate frequency-dependent contamination. The gradient-mode $X_{\ell m}^G$ bandpowers for all three frequency differences are shown in Figure 4. The 150–90 difference is the cleanest

TABLE I. Gradient-mode ($X_{\ell m}^G$) b_{ML} fits for all signal maps and footprints, over $2500 \leq \ell \leq 6000$ (6 log-spaced bins). PTE(gof): goodness-of-fit probability at best-fit b_{ML} . NGC+SGC values are obtained by inverse-variance weighting of per-cap bandpowers.

Map Footprint	$b_{\text{ML}} \pm \sigma$	Main			Extended				
		SNR	χ^2/dof	PTE(gof)	$b_{\text{ML}} \pm \sigma$	SNR	χ^2/dof	PTE(gof)	
<i>NILC</i>									
NGC+SGC	0.93 ± 0.25	3.7	1.03	0.40	1.24 ± 0.26	4.8	0.64	0.67	
NGC	0.94 ± 0.36	2.6	1.19	0.31	1.18 ± 0.33	3.6	0.90	0.48	
SGC	0.93 ± 0.36	2.6	1.21	0.30	1.33 ± 0.42	3.2	0.49	0.79	
<i>90 GHz</i>									
NGC+SGC	0.74 ± 0.35	2.1	0.68	0.64	0.93 ± 0.36	2.6	0.96	0.44	
NGC	0.75 ± 0.50	1.5	1.08	0.37	0.88 ± 0.46	1.9	0.74	0.59	
SGC	0.75 ± 0.49	1.5	0.71	0.62	1.01 ± 0.56	1.8	0.80	0.55	
<i>150 GHz</i>									
NGC+SGC	0.62 ± 0.31	2.0	0.73	0.60	1.14 ± 0.32	3.6	0.47	0.80	
NGC	0.85 ± 0.48	1.8	0.50	0.78	1.19 ± 0.43	2.8	0.45	0.82	
SGC	0.46 ± 0.42	1.1	1.18	0.31	1.07 ± 0.48	2.2	0.77	0.57	
<i>220 GHz</i>									
NGC+SGC	2.92 ± 1.28	2.3	0.46	0.80	3.08 ± 1.29	2.4	0.47	0.80	
NGC	3.66 ± 1.89	1.9	1.11	0.35	3.47 ± 1.60	2.2	0.79	0.56	
SGC	2.29 ± 1.74	1.3	0.99	0.42	2.32 ± 2.21	1.0	1.20	0.31	

blackbody null: for the main sample (NGC+SGC), $b_{\text{ML}} = -0.19 \pm 0.38$ ($p_0 = 0.62$, $\chi^2/\text{dof} = 0.48$); for the extended sample, $b_{\text{ML}} = +0.12 \pm 0.39$ ($p_0 = 0.76$, $\chi^2/\text{dof} = 0.94$). The NGC and SGC sub-regions are individually consistent with zero for both samples.

The 220–90 and 220–150 differences show positive amplitudes at 1.6–1.8 σ in the combined footprint. For the extended sample (NGC+SGC), 220–90 gives $b_{\text{ML}} = +2.17 \pm 1.30$ (1.7 σ , $p_0 = 0.09$) and 220–150 gives $+2.02 \pm 1.26$ (1.6 σ , $p_0 = 0.11$). For the main sample, 220–90 gives $+2.02 \pm 1.29$ (1.6 σ , $p_0 = 0.12$) and 220–150 gives $+2.28 \pm 1.25$ (1.8 σ , $p_0 = 0.07$). All SGC frequency differences are consistent with zero ($p_0 > 0.32$ for both samples).

All frequency-difference null tests pass at 2 σ (i.e. $0.05 < p_0 < 0.95$). Nevertheless, since the frequency-difference tests show the highest deviation from zero of any tests in our null test suite (up to 1.8 σ), and CMB foregrounds have been highlighted as a concern for moving-lens pipelines [19–21], we carry out additional foreground studies in §VI.

c. NGC–SGC footprint consistency. For each CMB map, we also show in Table II the difference between bandpowers of NGC and SGC as an additional systematics test; NILC gives $b_{\text{ML}}^{\text{NGC–SGC}} = -0.06 \pm 0.54$ ($p_0 = 0.92$) for the extended sample and $+0.03 \pm 0.51$ ($p_0 = 0.95$) for the main sample. The lowest p_0 across all eight NGC–SGC tests is 0.63, well above the 0.05 threshold.

d. Summary. Table II collects the null-test results for both samples across all footprints. We perform 25 null tests per sample: 4 curl-mode channels and 3 frequency differences, each evaluated on 3 footprints (NGC+SGC, NGC, SGC), plus 4 NGC–SGC consistency tests (one per CMB map). All null tests pass at 2 σ ($p_0 > 0.05$).

D. CMB map robustness checks

We test the sensitivity of our results to the inclusion of daytime data in the CMB co-add, and the treatment of high-noise regions at 220 GHz.

a. Daynight maps. ACT DR6 also provides daytime-plus-night co-adds, which have somewhat smaller noise but larger beam systematics on small scales. We analyze these maps to check their consistency with the night-only baseline used in this work. Across our six single-frequency (NGC+SGC) signal channels (90, 150 and 220 GHz, for the main and extended samples), shifts are typically of order $\mathcal{O}(0.1)$ sigma. No amplitude differs from the night-only baseline by more than 0.55 σ , with the largest shift at the 150 GHz extended (NGC+SGC): 1.30 ± 0.29 (daynight) vs 1.14 ± 0.32 (night-only). While the daynight per-frequency error bars are 9–15% smaller (the NILC maps, our tightest constraints, are produced from night-only maps), the daynight null tests show multiple main-sample deviations at $p_0 < 0.05$ including 220 GHz and NGC-involving difference tests, all returning to $p_0 > 0.05$ in the night-only baseline. The extended sample shows no $p_0 < 0.05$ entries in either configuration.

TABLE II. Null-test b_{ML} fits over $2500 \leq \ell \leq 6000$ (6 log-spaced bins). Curl-mode ($X_{\ell m}^C$) cross-spectra test for systematic contamination in the spin-1 decomposition; frequency-difference ($X_{\ell m}^G$) cross-spectra test for departures from blackbody frequency dependence; NGC+SGC ($X_{\ell m}^G$) tests consistency of the two galactic caps. All should yield $b_{\text{ML}} = 0$. PTE(gof): goodness-of-fit probability. p_0 : probability of the data under the null hypothesis of no signal. NGC+SGC values are obtained by inverse-variance weighting of per-cap bandpowers.

Map Footprint	$b_{\text{ML}} \pm \sigma$	Main				Extended					
		SNR	χ^2/dof	PTE(gof)	p_0	$b_{\text{ML}} \pm \sigma$	SNR	χ^2/dof	PTE(gof)	p_0	
<i>Curl mode ($X_{\ell m}^C$)</i>											
<i>NILC</i>											
NGC+SGC	$+0.14 \pm 0.25$	0.5	0.92	0.47	0.58	-0.11 ± 0.25	0.5	0.83	0.53	0.65	
NGC	-0.11 ± 0.36	0.3	0.50	0.78	0.77	-0.04 ± 0.33	0.1	0.50	0.78	0.90	
SGC	$+0.36 \pm 0.35$	1.0	1.45	0.20	0.30	-0.20 ± 0.38	0.5	0.76	0.58	0.59	
<i>90 GHz</i>											
NGC+SGC	$+0.41 \pm 0.35$	1.2	0.67	0.64	0.24	$+0.29 \pm 0.37$	0.8	0.83	0.53	0.43	
NGC	$+0.58 \pm 0.50$	1.2	0.42	0.83	0.25	$+0.82 \pm 0.48$	1.7	0.13	0.98	0.09	
SGC	$+0.24 \pm 0.48$	0.5	0.81	0.54	0.61	-0.43 ± 0.57	0.8	1.03	0.40	0.45	
<i>150 GHz</i>											
NGC+SGC	$+0.02 \pm 0.30$	0.1	0.82	0.54	0.95	-0.31 ± 0.31	1.0	1.01	0.41	0.31	
NGC	-0.38 ± 0.41	0.9	0.62	0.68	0.34	-0.41 ± 0.39	1.0	1.07	0.37	0.30	
SGC	$+0.48 \pm 0.44$	1.1	1.33	0.25	0.27	-0.17 ± 0.49	0.3	0.24	0.95	0.74	
<i>220 GHz</i>											
NGC+SGC	$+0.75 \pm 1.18$	0.6	1.52	0.18	0.52	$+0.14 \pm 1.25$	0.1	0.93	0.46	0.91	
NGC	$+0.66 \pm 1.66$	0.4	0.53	0.75	0.69	$+0.42 \pm 1.61$	0.3	1.08	0.37	0.79	
SGC	$+0.82 \pm 1.67$	0.5	1.64	0.14	0.62	-0.30 ± 1.98	0.2	1.60	0.16	0.88	
<i>Frequency differences ($X_{\ell m}^G$)</i>											
<i>150–90</i>											
NGC+SGC	-0.19 ± 0.38	0.5	0.48	0.79	0.62	$+0.12 \pm 0.39$	0.3	0.94	0.46	0.76	
NGC	$+0.14 \pm 0.54$	0.3	0.63	0.68	0.79	$+0.44 \pm 0.50$	0.9	0.43	0.83	0.38	
SGC	-0.54 ± 0.55	1.0	0.24	0.94	0.32	-0.37 ± 0.62	0.6	0.81	0.54	0.55	
<i>220–90</i>											
NGC+SGC	$+2.02 \pm 1.29$	1.6	0.48	0.79	0.12	$+2.17 \pm 1.30$	1.7	0.44	0.82	0.09	
NGC	$+2.77 \pm 1.84$	1.5	1.02	0.40	0.13	$+2.56 \pm 1.59$	1.6	0.73	0.60	0.11	
SGC	$+1.31 \pm 1.82$	0.7	0.88	0.49	0.47	$+1.40 \pm 2.27$	0.6	1.33	0.25	0.54	
<i>220–150</i>											
NGC+SGC	$+2.28 \pm 1.25$	1.8	0.43	0.83	0.07	$+2.02 \pm 1.26$	1.6	0.45	0.81	0.11	
NGC	$+2.86 \pm 1.78$	1.6	1.17	0.32	0.11	$+2.34 \pm 1.53$	1.5	0.78	0.56	0.13	
SGC	$+1.73 \pm 1.76$	1.0	0.88	0.49	0.33	$+1.36 \pm 2.22$	0.6	1.40	0.22	0.54	
<i>NGC+SGC ($X_{\ell m}^G$)</i>											
NILC	$+0.03 \pm 0.51$	0.1	1.39	0.22	0.95	-0.06 ± 0.54	0.1	0.77	0.57	0.92	
90 GHz	$+0.02 \pm 0.71$	0.0	1.11	0.35	0.98	-0.06 ± 0.73	0.1	0.60	0.70	0.94	
150 GHz	$+0.30 \pm 0.63$	0.5	0.99	0.42	0.63	$+0.06 \pm 0.65$	0.1	0.75	0.59	0.92	
220 GHz	$+1.16 \pm 2.61$	0.4	1.64	0.15	0.66	$+1.33 \pm 2.73$	0.5	1.50	0.19	0.63	

b. 220 GHz noise mask. The 220 GHz channel has the highest noise among the ACT frequency maps. We mask sky pixels where the 220 GHz white-noise level exceeds $300 \mu\text{K-arcmin}$, reducing the effective footprint by $\sim 10\%$. Across our six single-frequency (NGC+SGC) signal channels, amplitude shifts relative to the standard mask are small and mixed in sign, and the error bars are essentially unchanged ($\lesssim 10\%$ in either direction).

VI. FOREGROUND STUDIES

In Table II, the largest null-test deviations involve 220 GHz data, with amplitudes of 0.6–1.8 σ across the 220–90 and 220–150 frequency-difference rows. Given the number of null tests in our test suite, this level of tension is

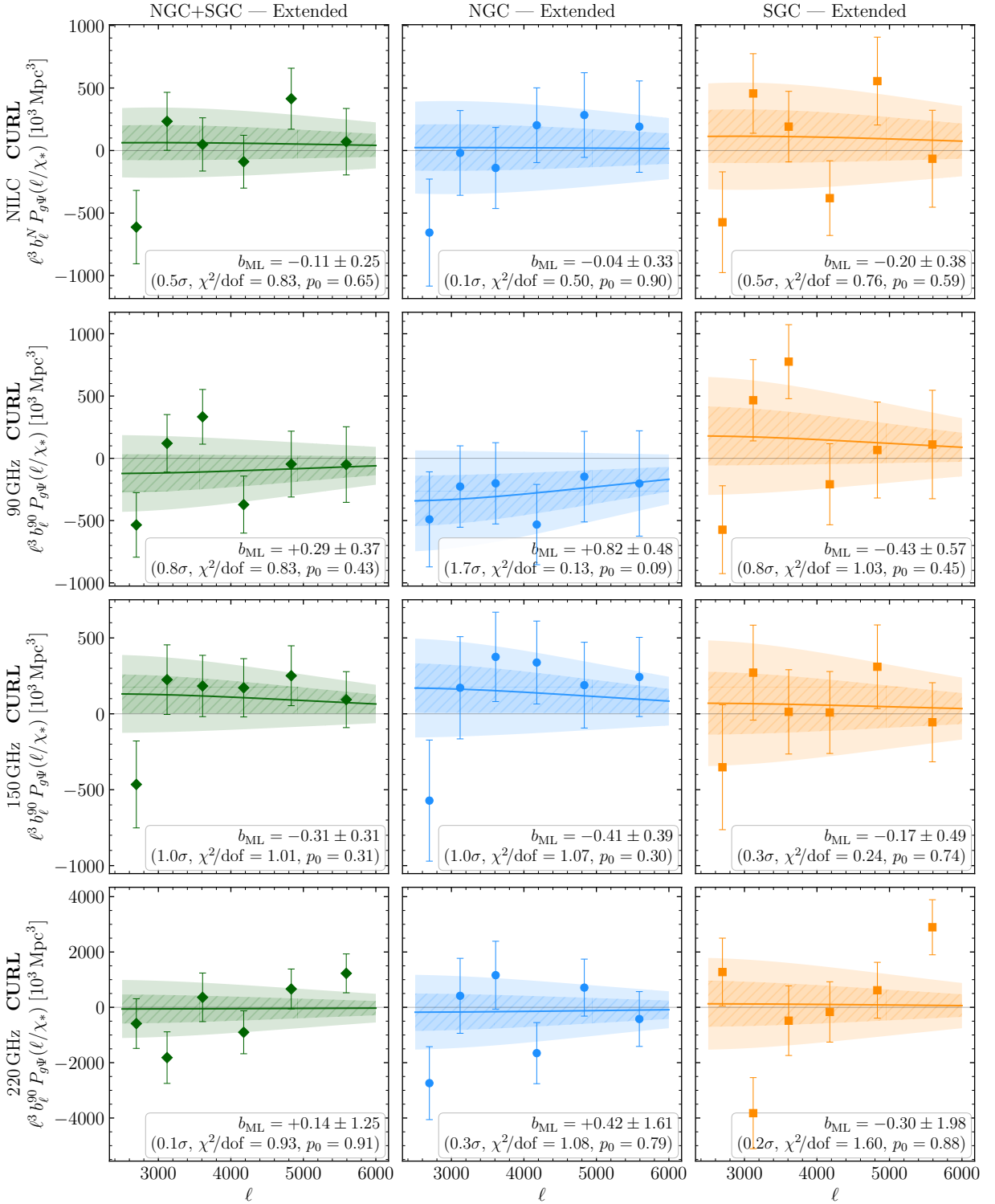


FIG. 3. The NILC and 90, 150 and 220 GHz bandpowers for the DESI-LS extended LRG sample. Panels show the *curl* mode $X_{\ell m}^C$. From left to right: NGC+SGC (inverse-variance weighted), NGC, SGC. Solid curves: best-fit b_{ML} template; darker hatched bands: 1σ ; lighter smooth bands: 2σ .

consistent with being a statistical fluke, but it motivated us to carry out two additional foreground studies, in order to increase confidence that foreground contamination is not an issue. The first test (§VI A) uses Planck 353/545 GHz data and is empirical, and the second test (§VI B) is based on simulations.

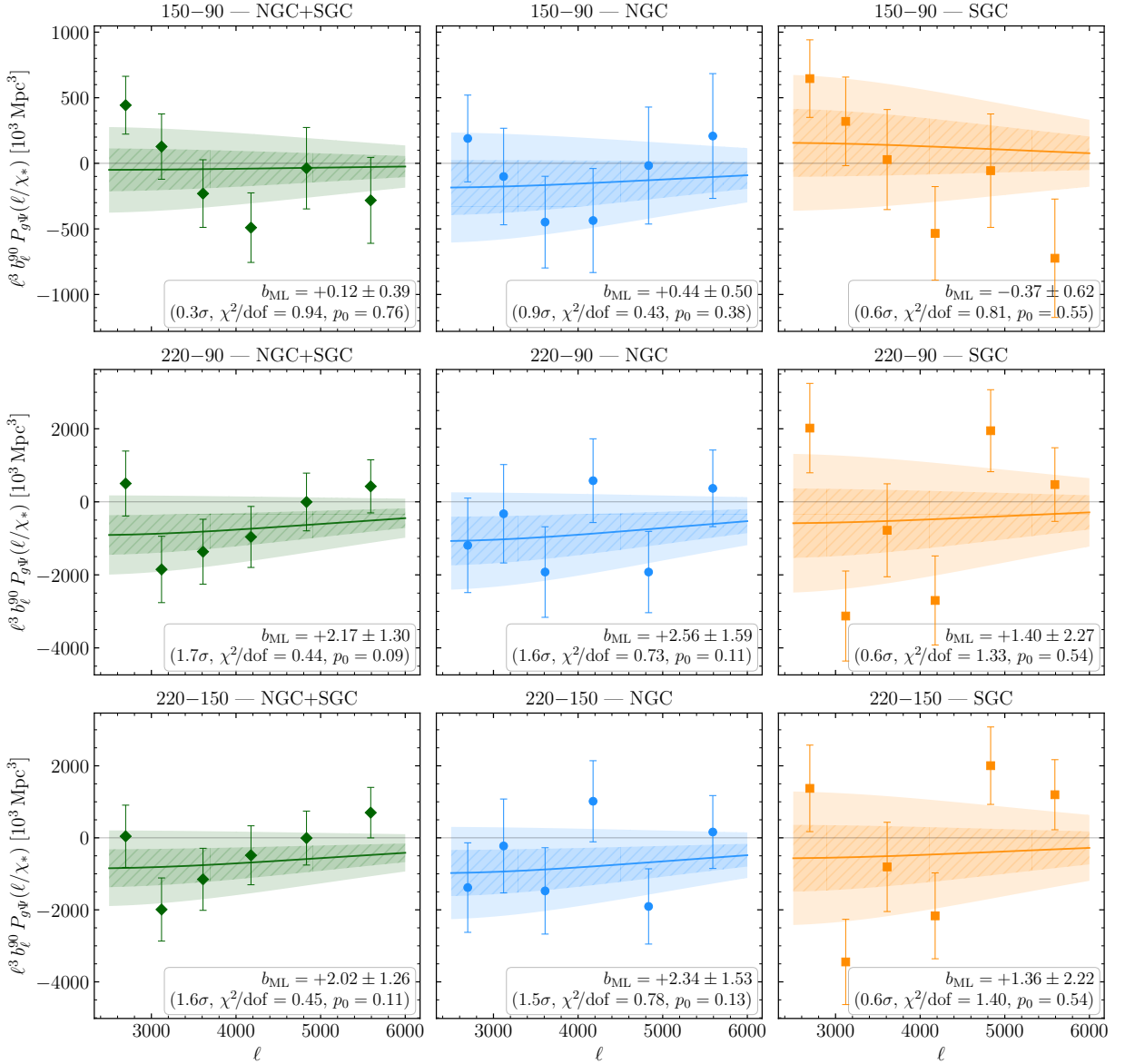


FIG. 4. Gradient-mode null-test bandpowers from frequency-difference maps for the DESI-LS extended LRG sample. Rows from top to bottom: 150–90, 220–90, 220–150. Columns from left to right: NGC+SGC combined, NGC, SGC. The 150–90 difference is consistent with zero for all footprints, as expected for a blackbody signal. Markers and bands as in Figures 2 and 3.

A. Constraints from Planck 353/545 GHz

The single-frequency amplitudes in Section VB show an elevated 220 GHz amplitude ($b_{\text{ML}} = 3.08 \pm 1.29$), and the frequency differences in Section VC yield 1.6–1.8 σ amplitudes for channels involving 220 GHz. To test whether this pattern reflects CIB contamination, we look at higher-frequency data. Planck NPIPE [29] provides full-sky temperature maps at frequencies up to 857 GHz, well above the ACT frequency range (90–220 GHz). The CIB spectral response rises steeply with frequency, making the Planck 353 and 545 GHz channels dominated by CIB contribution.

All results in this section use a more conservative angular mask, obtained from our default mask (see §IV B) by using the Planck GAL060 mask instead of GAL070. This more conservative mask mitigates Galactic dust contamination at 353/545 GHz. In particular, the “ACT 150” points in Figure 5 are slightly different from in the main paper, due to the different mask.

The Planck maps have higher noise and lower angular resolution than ACT. Nevertheless, the CIB is so bright at

353/545 GHz that Planck data can be used to estimate the CIB contribution to the ACT moving-lens signal at lower frequencies. We cross-correlate the NPIPE 353 and 545 GHz intensity maps, reprojected to the ACT pixell geometry, with the gradient mode $X_{\ell m}^G$ of the moving-lens template, obtaining a cross power spectrum $C_\ell^{\text{Planck} \times G}$. To compare this power spectrum to our ACT measurements, we rescale to predict the CIB contribution at 150 GHz in ACT:

$$C_\ell^{(\text{CIB } 150) \times G} = C_\ell^{(\text{Planck } \nu) \times G} \times \frac{f_{\text{CIB}}(150)}{f_{\text{CIB}}(\nu)} \times \frac{b_\ell^{90}}{b_\ell^\nu}, \quad (31)$$

where b_ℓ^{90} is the ACT 90 GHz beam transfer function (Section IV B) to which our ACT 150 GHz map (and all single-frequency ACT maps) is convolved (Eq. 29), and b_ℓ^ν is the NPIPE beam transfer function at frequency ν . We model the CIB spectral response $f_{\text{CIB}}(\nu)$ as a modified blackbody in CMB thermodynamic temperature units:

$$f_{\text{CIB}}(\nu) \propto \frac{\nu^{\beta_d} B(\nu, T_d)}{(\partial B / \partial T)_{T_{\text{CMB}}}}, \quad (32)$$

with $\beta_d = 1.7$ and $T_d = 10.7 \text{ K}$ following Ref. [26]. The spectral ratios are $f_{\text{CIB}}(150)/f_{\text{CIB}}(353) = 0.054$ and $f_{\text{CIB}}(150)/f_{\text{CIB}}(545) = 0.0037$.

To compute $C_\ell^{\text{Planck} \times G}$, we run the pipeline described in Section III, which consists of velocity reconstruction, surrogate-field normalization, and cross-spectrum computation; using the GAL060 galactic mask with 2° apodization to reduce Galactic dust contamination at 353 and 545 GHz. All derived products are computed self-consistently for this footprint. We bin in 6 bandpowers with $\Delta\ell = 500$ over $2000 \leq \ell \leq 5000$ and fit b_{ML} independently to the ACT 150 GHz cross-spectrum and to each Planck-derived CIB cross-spectrum. The upper multipole is lower than in the main analysis ($\ell_{\text{max}} = 6000$) because the Planck beam suppresses signal at high ℓ and these scales are dominated by noise in high-frequency maps. As before, NGC and SGC are combined via inverse-variance weighting at the bandpower level.

In Figure 5, we plot the quantity $C_\ell^{(\text{CIB } 150) \times G}$ defined in Eq. (31), converted to a measurement of $P_{g\Psi}(k)$ using Eq. (20). As explained above, this is a prediction for the CIB contribution to the ACT moving-lens signal at 150 GHz (assuming that 100% of the signal in the Planck 353/545 maps is CIB). Therefore, it can be compared directly to the ACT 150 GHz measurements (also shown in the plot).

The ACT 150 GHz cross-spectrum gives $b_{\text{ML}} = 1.06 \pm 0.27$ (3.9σ) for the combined footprint. The Planck-derived CIB cross-spectra give $b_{\text{ML}} = -0.07 \pm 0.14$ (0.5σ , 353 GHz) and -0.01 ± 0.10 (0.1σ , 545 GHz), both consistent with zero. NGC and SGC are individually consistent with zero: NGC gives -0.18 ± 0.22 (0.8σ) and $+0.21 \pm 0.15$ (1.4σ); SGC gives $+0.02 \pm 0.19$ (0.1σ) and -0.19 ± 0.14 (1.4σ).

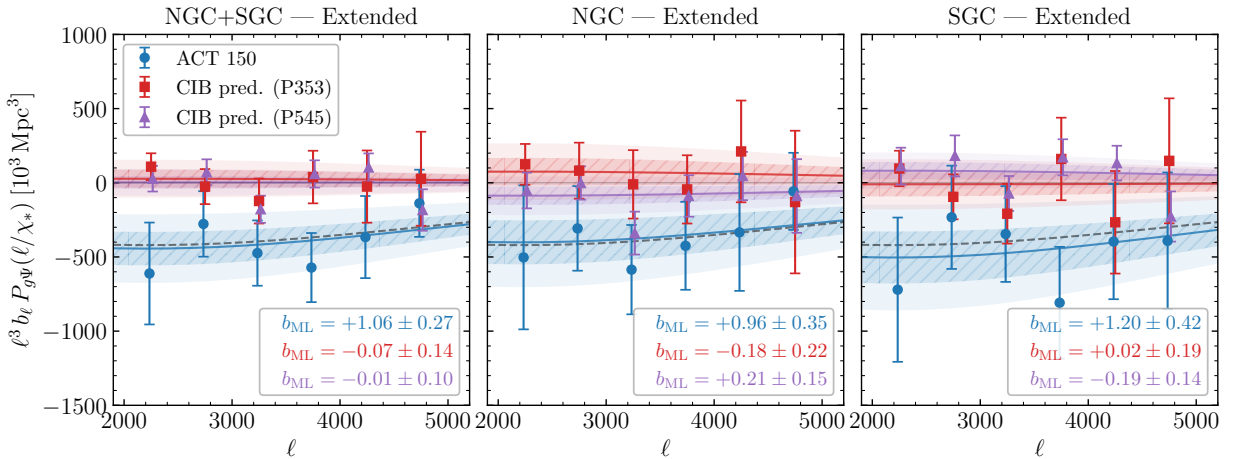


FIG. 5. Planck NPIPE 353 and 545 GHz cross-correlated with the velocity reconstruction, scaled to predict CIB contamination at 150 GHz (Eq. 31). Blue: ACT 150 GHz $\times X_{\ell m}^G$. Red/purple: Planck-derived CIB cross-spectra at 353/545 GHz. Solid curves: best-fit b_{ML} template; hatched-darker/lighter bands: $1\sigma/2\sigma$. Dashed line corresponds to $b_{\text{ML}} = 1$. From left to right: NGC+SGC, NGC, SGC. The analysis uses the GAL060 mask with 2° apodization, $\Delta\ell = 500$, $2000 \leq \ell \leq 5000$, and CIB spectral parameters $\beta_d = 1.7$, $T_d = 10.7 \text{ K}$ [26]. The legend in the first panel shows b_{ML} fits for the combined footprint; subsequent panels show per-cap values.

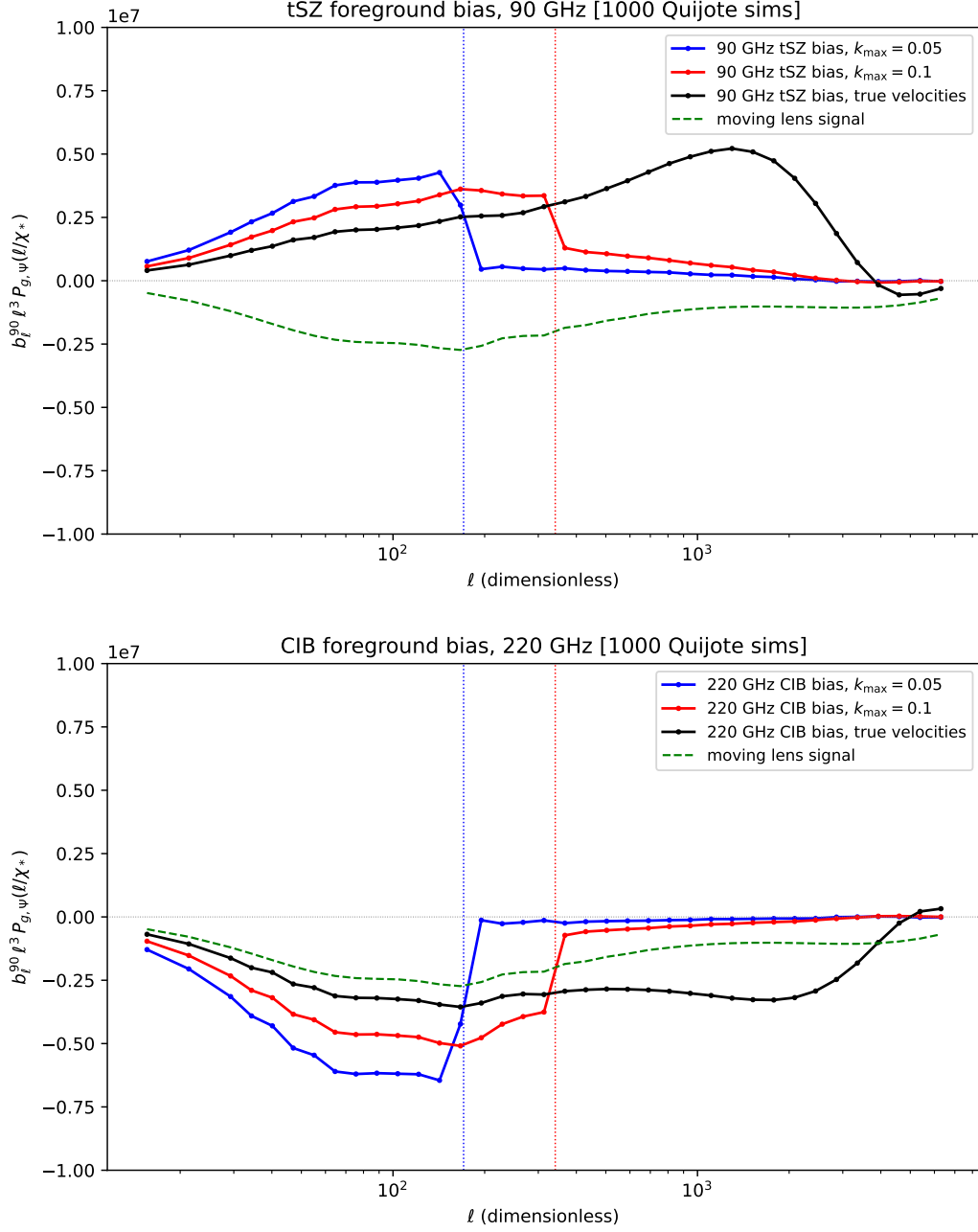


FIG. 6. Foreground bias to C_l^{TG} in a simplified Quijote-based pipeline at redshift $z_* = 1$. The top/bottom panels show the tSZ/CIB bias at the ACT frequency where the foreground is largest (90/220 GHz). The blue curves are most representative of our DESILS pipeline, where the velocity reconstruction contains a sharp cutoff at $k_{\max} = 0.05 \text{ Mpc}^{-1}$ (see Eq. (17)). We find that foreground biases are suppressed for $l \gtrsim k_{\max} \chi_* \approx 170$ (vertical lines), and smaller than the moving lens signal at high l . See text for more discussion.

Summarizing, when we use Planck 353/545 data to predict the CIB contamination to the ACT moving-lens signal, the results are consistent with zero contamination, with small error bars. Using 545 GHz data, we predict CIB bias $\Delta b_{\text{ML}} = 0.00 \pm 0.10$ (NGC+SGC extended) at 150 GHz, whereas the 150 GHz measured value is $b_{\text{ML}} = 1.06 \pm 0.27$. The CIB bias would be even smaller at 90 GHz. This is strong empirical evidence that our moving lens measurement is not affected by CIB.

B. Numerical results in a toy foreground model

To estimate the size of foreground biases to the moving-lens signal, we implemented a simplified pipeline based on Quijote simulations [30] and a toy foreground model. This simplified pipeline neglects significant complications (curved-sky, lightcone evolution, more realistic foregrounds) but should correctly predict the approximate size of foreground biases. We plan to do a more detailed study in future work. The details of the pipeline and foreground model are presented in Appendix C.

Our main result from this pipeline is shown in Figure 6. Recall that in our DESILS pipeline, the velocity reconstruction (see Eq. 17) contains a “sharp” cutoff at $k_{\max} = 0.05 \text{ Mpc}^{-1}$. In cases with a sharp cutoff, we find that foreground biases from both tSZ and CIB are dramatically suppressed for $l \gtrsim (k_{\max}\chi_*)$ (blue/red curves in Figure 6), and are small compared to the moving-lens signal (dashed green curve). (Note that the moving-lens signal in Figure 6 differs from the fiducial model elsewhere in the paper, since it was computed using halo model parameters (z, n_g^{3d}) appropriate for Quijote.)

This may be surprising, since previous simulation-based studies have shown that correlations between extragalactic foreground emission gradients (tSZ and CIB) and the transverse velocity field can produce contamination an order of magnitude larger than the ML signal on single-frequency maps [19–21]. Those analyses used true halo velocities from simulations; although they applied distortions to mimic reconstructed velocities [e.g. 20], they did not impose a scale cut on the velocity modes. By contrast, here we reconstruct velocities from the galaxy density field with a hard cutoff at $k_{\max} = 0.05 \text{ Mpc}^{-1}$. This cutoff produces a separation of scales: foreground contamination is significant at $\ell \lesssim k_{\max}\chi_* \approx 129$ but sharply drops to near zero at higher multipoles, well below our signal range ($\ell = 2500\text{--}6000$). On the other hand, if true halo velocities are used in the pipeline (black curve in Figure 6), then foreground contamination extends to high l . Intuitively, the small-scale physics of foreground emission is approximately uncorrelated with large-scale bulk motions, and therefore enforcing a clean separation of scales is sufficient to reduce the foregrounds to a negligible level.

Summarizing, we find that foreground bias to the moving-lens signal is predicted to be small in simulations, provided that two conditions are met:

1. The velocity reconstruction includes a “hard” cutoff at 3-d wavenumber k_{\max} , as in Eq. (C6). Note that for realistic parameter values, the threshold wavenumber $l_* = k_{\max}\chi_*$ is much smaller than “moving lens” values ($l \gtrsim 2500$). For example, if $k_{\max} = 0.05$ and $z_* = 0.7$, then $l_* = 129$.
2. The cross correlation with T is either done in Fourier space (C_l^{TG}) at $l \gg l_*$, or includes a low-pass filtering step to mitigate mixing from low l to high l .

In this paper, we have used an analysis pipeline which satisfies both of these conditions. Combining with results from §VI A, we have now shown that CMB foreground bias is expected to be **small compared to the moving-lens signal** in two ways: empirically (based on Planck 353/545 GHz data), and by comparing with simulations.

VII. DISCUSSION AND CONCLUSIONS

In this work, we have attained the first detection of the moving lens effect using a Fourier-space cross-spectrum estimator applied to ACT DR6 CMB temperature maps and luminous red galaxies from the DESI Legacy Imaging Surveys. The foreground-cleaned NILC map yields $b_{\text{ML}} = 1.24 \pm 0.26$ (4.8σ) for the extended sample and 0.93 ± 0.25 (3.7σ) for the main sample. The measured significance is consistent with the analytic forecast of $\text{SNR} = 3.7$ for $\text{ACT} \times 3.4\text{M}$ DESI LRGs obtained by Ref. [21]; our main and extended samples contain 5.1M and 13.2M galaxies, respectively, in the overlap region. The bandpower shape is consistent with the ML theory template at all frequencies, with goodness-of-fit probabilities exceeding 0.05 in all cases (Table I). We used two different methods to estimate statistical errors, both of which account for large-scale imaging systematics in DESILS, and find consistent results (Appendix B).

We performed a suite of null tests and other robustness checks (§V C, §V D). The largest null-test deviations involve ACT 220 GHz data, with amplitudes of $0.6\text{--}1.8\sigma$ across the 220–90 and 220–150 frequency-difference rows of Table II. This level of tension is consistent with being a statistical fluke, but it motivated us to carry out two additional foreground studies:

- In §VI A, we ran our moving-lens pipeline on Planck 353 and 545 GHz maps, in order to assess CIB contamination. No evidence for a signal $C_l^{TG} \neq 0$ was seen. Assuming that the 353/545 GHz maps are CIB-dominated,

we can rescale the Planck measurements to ACT frequencies, to estimate the level of CIB contamination in our main analysis. At 150 GHz, where $b_{\text{ML}} = 1.06 \pm 0.27$, we predict that the CIB bias is $\Delta b_{\text{ML}} = 0.00 \pm 0.10$. At 90 GHz, the CIB bias would be even smaller. This is strong empirical evidence that our moving lens measurement is not affected significantly by CIB. (In this study, we focused on CIB instead of tSZ since the 90-150 null tests all pass at $< 1\sigma$; see Table II.)

- In §VIB, we measured CMB foreground bias in a simplified simulation pipeline, based on Quijote simulations and toy models for CMB foregrounds. We found that both tSZ and CIB biases are small compared to the moving lens signal (Figure 6), and explained why this result is consistent with previous simulation-based studies [19–21]. This is strong simulation-based evidence that our moving lens measurement is not affected significantly by either tSZ or CIB.

The Simons Observatory [14] will provide lower-noise CMB maps with improved angular resolution, increasing the per-channel SNR and adding a fourth independent frequency for foreground separation. In future work, we will use DESI spectroscopic redshifts in place of photometric estimates, improving both the velocity reconstruction and the theory template accuracy. Beheshti et al. [21] forecast SNR ~ 8 –10 for SO \times DESI Y5 with the moving lens effect, which would enable tighter constraints on both the signal amplitude and the foreground parameters. Natural extensions include realistic foreground simulations with k_{max} -limited velocity reconstruction, template deprojection [21], and ILC maps with explicit tSZ or CIB nulling.

The moving lens effect probes the transverse velocity field of large-scale structure—a quantity not directly accessible to kSZ and galaxy clustering measurements, which are sensitive only to radial velocities and density perturbations, respectively. Combined with radial velocity information from kSZ tomography [24], the cross-spectrum approach developed here can be extended to upcoming surveys to constrain $f\sigma_8$ through the transverse velocity field [8], complementing existing probes based on radial velocities.

ACKNOWLEDGMENTS

We thank Boryana Hadzhiyska, Gil Holder and Rongpu Zhou for very useful discussions. SCH was supported by the P. J. E. Peebles Fellowship at Perimeter Institute. KMS was supported by an NSERC Discovery Grant, by the Daniel Family Foundation, and by the Centre for the Universe at Perimeter Institute. Research at Perimeter Institute is supported by the Government of Canada through Industry Canada and by the Province of Ontario through the Ministry of Research & Innovation. SF is supported by Lawrence Berkeley National Laboratory and the Director, Office of Science, Office of High Energy Physics of the U.S. Department of Energy under Contract No. DE-AC02-05CH11231. This research was supported in part by grant NSF PHY-2309135 to the Kavli Institute for Theoretical Physics (KITP).

We acknowledge the use of public data from ACT and the DESI Legacy Imaging Surveys made available through the National Energy Research Scientific Computing Center (NERSC), a U.S. Department of Energy Office of Science User Facility operated under Contract No. DE-AC02-05CH11231.

The Legacy Surveys consist of three individual and complementary projects: the Dark Energy Camera Legacy Survey (DECaLS; Proposal ID 2014B-0404; PIs: David Schlegel and Arjun Dey), the Beijing-Arizona Sky Survey (BASS; NOAO Prop. ID 2015A-0801; PIs: Zhou Xu and Xiaohui Fan), and the Mayall z-band Legacy Survey (MzLS; Prop. ID 2016A-0453; PI: Arjun Dey). DECaLS, BASS and MzLS together include data obtained, respectively, at the Blanco telescope, Cerro Tololo Inter-American Observatory, NSF’s NOIRLab; the Bok telescope, Steward Observatory, University of Arizona; and the Mayall telescope, Kitt Peak National Observatory, NOIRLab. Pipeline processing and analyses of the data were supported by NOIRLab and the Lawrence Berkeley National Laboratory (LBNL). The Legacy Surveys project is honored to be permitted to conduct astronomical research on Iolkam Du’ag (Kitt Peak), a mountain with particular significance to the Tohono O’odham Nation.

NOIRLab is operated by the Association of Universities for Research in Astronomy (AURA) under a cooperative agreement with the National Science Foundation. LBNL is managed by the Regents of the University of California under contract to the U.S. Department of Energy.

This project used data obtained with the Dark Energy Camera (DECam), which was constructed by the Dark Energy Survey (DES) collaboration. Funding for the DES Projects has been provided by the U.S. Department of Energy, the U.S. National Science Foundation, the Ministry of Science and Education of Spain, the Science and Technology Facilities Council of the United Kingdom, the Higher Education Funding Council for England, the National Center for Supercomputing Applications at the University of Illinois at Urbana-Champaign, the Kavli Institute of

Cosmological Physics at the University of Chicago, Center for Cosmology and Astro-Particle Physics at the Ohio State University, the Mitchell Institute for Fundamental Physics and Astronomy at Texas A&M University, Financiadora de Estudos e Projetos, Fundacao Carlos Chagas Filho de Amparo a Pesquisa do Estado do Rio de Janeiro, Conselho Nacional de Desenvolvimento Cientifico e Tecnologico and the Ministerio da Ciencia, Tecnologia e Inovacao, the Deutsche Forschungsgemeinschaft and the Collaborating Institutions in the Dark Energy Survey. The Collaborating Institutions are Argonne National Laboratory, the University of California at Santa Cruz, the University of Cambridge, Centro de Investigaciones Energeticas, Medioambientales y Tecnologicas-Madrid, the University of Chicago, University College London, the DES-Brazil Consortium, the University of Edinburgh, the Eidgenossische Technische Hochschule (ETH) Zurich, Fermi National Accelerator Laboratory, the University of Illinois at Urbana-Champaign, the Institut de Ciencies de l'Espai (IEEC/CSIC), the Institut de Fisica d'Altes Energies, Lawrence Berkeley National Laboratory, the Ludwig Maximilians Universitat Munchen and the associated Excellence Cluster Universe, the University of Michigan, NSF's NOIRLab, the University of Nottingham, the Ohio State University, the University of Pennsylvania, the University of Portsmouth, SLAC National Accelerator Laboratory, Stanford University, the University of Sussex, and Texas A&M University.

BASS is a key project of the Telescope Access Program (TAP), which has been funded by the National Astronomical Observatories of China, the Chinese Academy of Sciences (the Strategic Priority Research Program “The Emergence of Cosmological Structures” Grant # XDB09000000), and the Special Fund for Astronomy from the Ministry of Finance. The BASS is also supported by the External Cooperation Program of Chinese Academy of Sciences (Grant # 114A11KYSB20160057), and Chinese National Natural Science Foundation (Grant # 12120101003, # 11433005).

The Legacy Survey team makes use of data products from the Near-Earth Object Wide-field Infrared Survey Explorer (NEOWISE), which is a project of the Jet Propulsion Laboratory/California Institute of Technology. NEOWISE is funded by the National Aeronautics and Space Administration.

The Legacy Surveys imaging of the DESI footprint is supported by the Director, Office of Science, Office of High Energy Physics of the U.S. Department of Energy under Contract No. DE-AC02-05CH11231, by the National Energy Research Scientific Computing Center, a DOE Office of Science User Facility under the same contract; and by the U.S. National Science Foundation, Division of Astronomical Sciences under Contract No. AST-0950945 to NOAO.

-
- [1] A. G. Adame *et al.* (DESI), DESI 2024 VII: Cosmological Constraints from the Full-Shape Modeling of Clustering Measurements, arXiv e-prints (2024), [arXiv:2411.12022 \[astro-ph.CO\]](#).
 - [2] R. A. Sunyaev and Y. B. Zeldovich, The Velocity of clusters of galaxies relative to the microwave background. The Possibility of its measurement, *Mon. Not. Roy. Astron. Soc.* **190**, 413 (1980).
 - [3] N. Hand *et al.*, Evidence of Galaxy Cluster Motions with the Kinematic Sunyaev-Zel'dovich Effect, *Physical Review Letters* **109**, 041101 (2012).
 - [4] F. D. Bernardis *et al.*, Detection of the pairwise kinematic Sunyaev-Zel'dovich effect with BOSS DR11 and the Atacama Cosmology Telescope, *Journal of Cosmology and Astroparticle Physics* **2017** (03), 008.
 - [5] E. Schaan *et al.* (ACTPol), Evidence for the kinematic Sunyaev-Zel'dovich effect with the Atacama Cosmology Telescope and velocity reconstruction from the Baryon Oscillation Spectroscopic Survey, *Phys. Rev. D* **93**, 082002 (2016), [arXiv:1510.06442 \[astro-ph.CO\]](#).
 - [6] K. M. Smith, M. S. Madhavacheril, M. Münchmeyer, S. Ferraro, U. Giri, and M. C. Johnson, KSZ tomography and the bispectrum, arXiv e-prints, arXiv:1810.13423 (2018), [arXiv:1810.13423 \[astro-ph.CO\]](#).
 - [7] N. Dalal, O. Dore, D. Huterer, and A. Shirokov, The imprints of primordial non-gaussianities on large-scale structure: scale dependent bias and abundance of virialized objects, *Phys. Rev. D* **77**, 123514 (2008), [arXiv:0710.4560 \[astro-ph\]](#).
 - [8] S. C. Hotinli, K. M. Smith, M. S. Madhavacheril, and M. Kamionkowski, Cosmology with the moving lens effect, *Phys. Rev. D* **104**, 083529 (2021), [arXiv:2108.02207 \[astro-ph.CO\]](#).
 - [9] M. Birkinshaw and S. F. Gull, A test for transverse motions of clusters of galaxies, *Nature (London)* **302**, 315 (1983).
 - [10] N. Aghanim, S. Prunet, O. Forni, and F. R. Bouchet, Moving gravitational lenses: Imprints on the CMB, Submitted to: *Astron. Astrophys.* (1998), [*Astron. Astrophys.*334,409(1998)], [arXiv:astro-ph/9803040 \[astro-ph\]](#).
 - [11] R. K. Sachs and A. M. Wolfe, Perturbations of a Cosmological Model and Angular Variations of the Microwave Background, *Astrophys. J.* **147**, 73 (1967).
 - [12] M. J. Rees and D. W. Sciama, Large-scale Density Inhomogeneities in the Universe, *Nature (London)* **217**, 511 (1968).
 - [13] S. C. Hotinli, J. Meyers, N. Dalal, A. H. Jaffe, M. C. Johnson, J. B. Mertens, M. Münchmeyer, K. M. Smith, and A. van Engelen, Transverse Velocities with the Moving Lens Effect, *Phys. Rev. Lett.* **123**, 061301 (2019), [arXiv:1812.03167 \[astro-ph.CO\]](#).
 - [14] P. Ade *et al.* (Simons Observatory), The Simons Observatory: Science goals and forecasts, *JCAP* **02**, 056, [arXiv:1808.07445 \[astro-ph.CO\]](#).

- [15] P. A. Abell *et al.* (LSST Science, LSST Project), LSST Science Book, Version 2.0, arXiv e-prints (2009), [arXiv:0912.0201 \[astro-ph.IM\]](#).
- [16] S. C. Hotinli, M. C. Johnson, and J. Meyers, Optimal filters for the moving lens effect, *Phys. Rev. D* **103**, 043536 (2021), [arXiv:2006.03060 \[astro-ph.CO\]](#).
- [17] S. Yasini, N. Mirzatury, and E. Pierpaoli, Pairwise Transverse Velocity Measurement with the Rees-Sciama Effect, *Astrophys. J. Lett.* **873**, L23 (2019), [arXiv:1812.04241 \[astro-ph.CO\]](#).
- [18] A. Obuljen, W. J. Percival, and N. Dalal, Detection of anisotropic galaxy assembly bias in BOSS DR12, *JCAP* **10**, 058, [arXiv:2004.07240 \[astro-ph.CO\]](#).
- [19] S. C. Hotinli, E. Pierpaoli, S. Ferraro, and K. Smith, Transverse velocities and matter gradient correlations: a new signal and a new challenge to moving-lens analyses, arXiv e-prints (2023), [arXiv:2305.15462 \[astro-ph.CO\]](#).
- [20] S. C. Hotinli and E. Pierpaoli, On the detectability of the moving lens signal in CMB experiments, *JCAP* **06**, 076, [arXiv:2401.12280 \[astro-ph.CO\]](#).
- [21] A. Beheshti, E. Schaan, and A. Kosowsky, The Moving Lens Effect: Simulations, Forecasts and Foreground Mitigation, arXiv e-prints (2024), [arXiv:2408.16055 \[astro-ph.CO\]](#).
- [22] B. R. Guachalla, E. Schaan, B. Hadzhiyska, and S. Ferraro, Velocity reconstruction in the era of DESI and Rubin/LSST. I. Exploring spectroscopic, photometric, and hybrid samples, *Phys. Rev. D* **109**, 103533 (2024), [arXiv:2312.12435 \[astro-ph.CO\]](#).
- [23] B. Hadzhiyska, S. Ferraro, B. R. Guachalla, and E. Schaan, Velocity reconstruction in the era of DESI and Rubin/LSST. II. Realistic samples on the light cone, *Phys. Rev. D* **109**, 103534 (2024), [arXiv:2312.12434 \[astro-ph.CO\]](#).
- [24] S. C. Hotinli, K. M. Smith, and S. Ferraro, Velocity Reconstruction from KSZ: Measuring f_{NL} with ACT and DESILS, arXiv e-prints (2025), [arXiv:2506.21657 \[astro-ph.CO\]](#).
- [25] S. Naess *et al.*, The Atacama Cosmology Telescope: arcminute-resolution maps of 18 000 square degrees of the microwave sky from ACT 2008–2018 data combined with Planck, *JCAP* **12**, 046, [arXiv:2007.07290 \[astro-ph.IM\]](#).
- [26] W. Coulton *et al.* (ACT), Atacama Cosmology Telescope: High-resolution component-separated maps across one third of the sky, *Phys. Rev. D* **109**, 063530 (2024), [arXiv:2307.01258 \[astro-ph.CO\]](#).
- [27] A. Aghamousa *et al.* (DESI), The DESI Experiment Part I: Science, Targeting, and Survey Design, arXiv e-prints (2016), [arXiv:1611.00036 \[astro-ph.IM\]](#).
- [28] R. Zhou *et al.* (DESI), Target Selection and Validation of DESI Luminous Red Galaxies, *Astron. J.* **165**, 58 (2023), [arXiv:2208.08515 \[astro-ph.CO\]](#).
- [29] Y. Akrami *et al.* (Planck), *Planck* intermediate results. LVII. Joint Planck LFI and HFI data processing, *Astron. Astrophys.* **643**, A42 (2020), [arXiv:2007.04997 \[astro-ph.CO\]](#).
- [30] F. Villaescusa-Navarro *et al.*, The Quijote simulations, *Astrophys. J. Suppl.* **250**, 2 (2020), [arXiv:1909.05273 \[astro-ph.CO\]](#).
- [31] A. S. Maniyar, M. Béthermin, and G. Lagache, Simple halo model formalism for the cosmic infrared background and its correlation with the thermal Sunyaev-Zel’dovich effect, *Astron. Astrophys.* **645**, A40 (2021), [arXiv:2006.16329 \[astro-ph.CO\]](#).
- [32] L. Harscouet, K. Wolz, A. Wayland, D. Alonso, and B. Hadzhiyska, kSZ for everyone: the pseudo-Cl approach to stacking, arXiv e-prints (2025), [arXiv:2512.14625 \[astro-ph.CO\]](#).
- [33] F. J. Qu *et al.*, Precision Kinematic Sunyaev–Zel’dovich Measurements Across Halo Mass and Redshift with DESI DR2 and ACT DR6: Part I. Luminous Red Galaxies, arXiv e-prints (2026), [arXiv:2604.19744 \[astro-ph.CO\]](#).
- [34] B. Hadzhiyska *et al.*, Precision Kinematic Sunyaev–Zel’dovich Measurements Across Halo Mass and Redshift with DESI DR2 and ACT DR6: Part II. Bright Galaxy Survey and Emission-Line Galaxies, arXiv e-prints (2026), [arXiv:2604.19745 \[astro-ph.CO\]](#).
- [35] M. S. Madhavacheril, N. Battaglia, K. M. Smith, and J. L. Sievers, Cosmology with the kinematic Sunyaev-Zeldovich effect: Breaking the optical depth degeneracy with fast radio bursts, *Phys. Rev. D* **100**, 103532 (2019), [arXiv:1901.02418 \[astro-ph.CO\]](#).
- [36] B. Hadzhiyska, S. Ferraro, G. S. Farren, N. Sailer, and R. Zhou, Missing baryons recovered: A measurement of the gas fraction in galaxies and groups with the kinematic Sunyaev-Zel’dovich effect and CMB lensing, *Phys. Rev. D* **112**, 123507 (2025), [arXiv:2507.14136 \[astro-ph.CO\]](#).
- [37] A. Dey *et al.*, Overview of the DESI Legacy Imaging Surveys, *AJ* **157**, 168 (2019), [arXiv:1804.08657 \[astro-ph.IM\]](#).
- [38] R. Zhou *et al.*, DESI luminous red galaxy samples for cross-correlations, *JCAP* **11**, 097, [arXiv:2309.06443 \[astro-ph.CO\]](#).
- [39] M. White *et al.*, Cosmological constraints from the tomographic cross-correlation of DESI Luminous Red Galaxies and Planck CMB lensing, *JCAP* **02** (02), 007, [arXiv:2111.09898 \[astro-ph.CO\]](#).
- [40] B. Hadzhiyska, S. Ferraro, *et al.*, Evidence for large baryonic feedback at low and intermediate redshifts from kinematic Sunyaev-Zel’dovich observations with ACT and DESI photometric galaxies, *Phys. Rev. D* **112**, 083509 (2025), [arXiv:2407.07152 \[astro-ph.CO\]](#).
- [41] S. Naess *et al.* (ACT), The Atacama Cosmology Telescope: DR6 maps, *JCAP* **2025** (11), 061, [arXiv:2503.14451 \[astro-ph.CO\]](#).
- [42] Planck Collaboration, Planck 2015 results. XLVIII. An overview of the GNILC method applied to polarized thermal dust emission, *Astron. Astrophys.* **596**, A109 (2016), [arXiv:1605.09387 \[astro-ph.CO\]](#).
- [43] A. R. Duffy, J. Schaye, S. T. Kay, and C. Dalla Vecchia, Dark matter halo concentrations in the Wilkinson Microwave Anisotropy Probe year 5 cosmology, *Mon. Not. Roy. Astron. Soc.* **390**, L64 (2008), [Erratum: *Mon. Not. Roy. Astron. Soc.*

415, L85 (2011)], [arXiv:0804.2486](https://arxiv.org/abs/0804.2486) [astro-ph].

Appendix A: Normalization and surrogate fields

In this appendix, we derive Eq. (20), which shows how C_ℓ^{TG} and $P_{g\Psi}(k)$ are related in our full pipeline from §III B. To compute C_ℓ^{TG} , we assume that each small subvolume ($d\Omega d\chi$) makes a contribution dC_ℓ^{TG} which is given by Eq. (13) from our simplified pipeline:

$$\begin{aligned} dC_\ell^{TG} &\approx \ell b_\ell \frac{\eta_\perp(\mathbf{x}) n_g^{3d}(\mathbf{x}) T_{\text{CMB}} d\chi}{\chi} \frac{d\Omega}{4\pi} P_{g\Psi}(\chi, k)_{k=\ell/\chi} \\ &= \ell b_\ell \frac{\eta_\perp(\mathbf{x}) T_{\text{CMB}}}{4\pi \chi^3} \left(n_g^{3d}(\mathbf{x}) \chi^2 d\chi d\Omega \right) P_{g\Psi}(\chi, k)_{k=\ell/\chi}. \end{aligned} \quad (\text{A1})$$

Here, $n_g^{3d}(\mathbf{x})$ is the weighted (i.e. including the galaxy weight W_i from Eq. (18)) comoving galaxy density near \mathbf{x} . The quantity $\eta_\perp(\mathbf{x})$ was defined in Eq. (21). The factor $f_{\text{sky}} = (d\Omega/4\pi)$ in the first line arises because C_ℓ^{TG} denotes the ‘‘pseudo’’ (not f_{sky} -scaled) full sky power spectrum. The total moving-lens contribution to C_ℓ^{TG} is given by integrating (A1) over subvolumes:

$$C_\ell^{TG} \approx \ell b_\ell \frac{T_{\text{CMB}}}{4\pi} \int \left(n_g^{3d}(\mathbf{x}) \chi^2 d\chi d\Omega \right) \frac{\eta_\perp(\mathbf{x})}{\chi^3} P_{g\Psi}(\chi, k)_{k=\ell/\chi}. \quad (\text{A2})$$

The level of approximation here is similar to the Limber approximation, combined with the approximation that pseudo power spectra scale as f_{sky} , rather than keeping track of the full pseudo- C_ℓ mixing matrix. (The Limber approximation lets us compute C_ℓ^{TG} one radial slice $d\chi$ at a time, and the latter approximation lets us compute it one angular element $d\Omega$ at a time.)

We approximate the integral $\int (n_g^{3d} \chi^2 d\chi d\Omega)(\dots)$ by a sum over galaxies $\sum_i(\dots)$:

$$C_\ell^{TG} \approx \ell b_\ell \frac{T_{\text{CMB}}}{4\pi} \sum_{i \in \text{gal}} W_i \frac{\eta_\perp(\mathbf{x}_i)}{\chi_i^3} P_{g\Psi}(\chi_i, k)_{k=\ell/\chi_i}. \quad (\text{A3})$$

In the effective redshift approximation $P_{g\Psi}(\chi_i, k)_{k=\ell/\chi_i} \approx P_{g\Psi}(\chi_*, k)_{k=\ell/\chi_*}$, we can write the result as:

$$C_\ell^{TG} \approx \ell b_\ell \mathcal{N} P_{g\Psi}(\chi_*, k)_{k=\ell/\chi_*} \quad \text{where } \mathcal{N} \equiv \frac{T_{\text{CMB}}}{4\pi} \sum_{i \in \text{gal}} W_i \frac{\eta_\perp(\mathbf{x}_i)}{\chi_i^3}. \quad (\text{A4})$$

This is the first main result of this appendix, and was given in the main text as Eq. (20).

So far, we have written the normalization \mathcal{N} in terms of the quantity

$$\eta_\perp(\mathbf{x}) \equiv \left\langle v_a^{\text{true}}(\mathbf{x}) \hat{v}_a(\mathbf{x}) \right\rangle, \quad (\text{A5})$$

but we have not explained how to compute $\eta_\perp(\mathbf{x})$. In the rest of this appendix, we will give an efficient algorithm.

In principle, $\eta_\perp(\mathbf{x})$ could be computed using mock simulations of DESILS, since it is defined as an expectation value over mocks. However, following [24], we can simplify dramatically by using ‘‘surrogate’’ simulations instead of mocks. By definition, a surrogate field is a field $S_g(\mathbf{x})$ that has the same large-scale 2PCF as the galaxy field $\rho_g(\mathbf{x})$, but can be constructed in whatever way is convenient.

In [24], we show in detail how to construct a surrogate field $S_g(\mathbf{x})$ for DESILS, by starting with a Gaussian field $\delta_{\text{lin}}(\mathbf{x})$ in the bounding box, and ‘‘painting’’ values of $\delta_{\text{lin}}(\mathbf{x})$ onto randoms as follows:

$$S_g(\mathbf{x}) = \frac{N_g}{N_r} \sum_{\beta \in \text{rand}} W_\beta b_g \delta_{\text{lin}}(\mathbf{x}_\beta^{\text{true}}) \delta^3(\mathbf{x} - \mathbf{x}_\beta^{\text{obs}}), \quad (\text{A6})$$

where δ_{lin} is a realization of a Gaussian random field drawn from the linear matter power spectrum $P_{\text{lin}}(k)$, and the factor b_g converts matter to galaxy overdensity on linear scales. Each object in the random catalog has two 3-d locations ($\mathbf{x}_j^{\text{true}}, \mathbf{x}_j^{\text{obs}}$), obtained using its true and observed (i.e. including photo- z error) redshifts.

The true and reconstructed velocities in the surrogate simulation are:

$$v_j^{\text{true}}(\mathbf{x}) = \int \frac{d^3\mathbf{k}}{(2\pi)^3} (ik_j) \frac{faH}{k^2} e^{i\mathbf{k}\cdot\mathbf{x}} \delta_{\text{lin}}(\mathbf{k}), \quad (\text{A7})$$

$$\hat{v}_j(\mathbf{x}) = \int \frac{d^3\mathbf{k}}{(2\pi)^3} (ik_j) U(k) e^{i\mathbf{k}\cdot\mathbf{x}} S_g(\mathbf{k}), \quad (\text{A8})$$

where $U(k)$ was defined in Eq. (17). The normalization \mathcal{N} is estimated by replacing the galaxy sum in Eq. (A4) with a sum over random catalog positions, using surrogate fields to estimate $\eta_{\perp}(\mathbf{x}) \equiv \langle v_a^{\text{true}}(\mathbf{x}) \hat{v}_a(\mathbf{x}) \rangle$:

$$\mathcal{N} \approx \frac{T_{\text{CMB}}}{4\pi} \frac{N_g}{N_r} \sum_{\beta \in \text{rand}} W_{\beta} \frac{\sum_a v_a^{\text{true}}(\mathbf{x}_{\beta}^{\text{true}}) \hat{v}_a(\mathbf{x}_{\beta}^{\text{obs}})}{\chi_{\beta}^3}. \quad (\text{A9})$$

This is the second main result of this appendix, and shows how to estimate the normalization \mathcal{N} via a Monte Carlo procedure involving Gaussian random fields and the random catalog.

For more details on surrogate simulations, including a formal proof that they have the same large-scale 2PCF as the data, see [24] (§III and Appendix B). In this context, a key point is that $\eta_{\perp}(\mathbf{x})$ only depends on the large-scale 2PCF of the mocks, since the RHS of (A5) only depends on large-scale modes of $v_a^{\text{true}}(\mathbf{x})$ and $\hat{v}_a(\mathbf{x})$, which are both linear in $\delta_g(\mathbf{x})$. Therefore, $\eta_{\perp}(\mathbf{x})$ can be computed using surrogate fields.

In practice, we average over N_{MC} independent Gaussian realizations to reduce scatter:

$$\mathcal{N} \approx \frac{1}{N_{\text{MC}}} \sum_{n=1}^{N_{\text{MC}}} \mathcal{N}^{(n)}, \quad (\text{A10})$$

where each $\mathcal{N}^{(n)}$ is computed from the n -th surrogate realization. We use $N_{\text{MC}} = 50$ throughout this work, which suffices for a percent-level measurement of \mathcal{N} (the scatter between simulations is small).

Appendix B: Simulation-based method for assigning error bars

In §III C, we assigned error bars to C_{ℓ}^{TG} using an “empirical” estimator (Eq. 23) based on the level of scatter between ℓ -values. As a check, we also implemented an alternate, simulation-based procedure for assigning error bars, and verified that the two methods give nearly identical results. In this appendix, we describe our alternate, simulation-based method.

Setting up a simulation pipeline is nontrivial, since there is no publicly available set of high-fidelity simulations for either ACT or DESILS. Note that C_{ℓ}^{TG} is a three-way correlation between the small-scale galaxy field, the large-scale velocity reconstruction $\hat{v}_a(\boldsymbol{\theta})$, and the small-scale CMB temperature. It would suffice to simulate any one of these three factors (leaving the other two fixed to their “data” values), but each one is challenging to simulate for different reasons:

- Simulating the small-scale DESILS galaxy field depends on detailed HOD modelling, which is astrophysically uncertain and difficult to fit from data.
- Conversely, in order to simulate $\hat{v}_a(\boldsymbol{\theta})$, we need to simulate large-scale modes of DESILS. This is straightforward from a physics perspective (we just need linear theory + photo- z errors), but DESILS has systematic power on large scales which is non-negligible compared to the clustering signal.
- Simulating the small-scale CMB is challenging, since it depends on both foreground modelling and ACT noise modelling.

Our approach is to simulate $\hat{v}_a(\boldsymbol{\theta})$ (middle bullet point), but correct for large-scale systematic power by rescaling by an overall constant A that we fit from data. In more detail, our simulation method is as follows:

1. In each Monte Carlo iteration, we simulate $\hat{v}_a(\boldsymbol{\theta})$ using the surrogate method from Appendix A (see Eq. A7).

We construct an X -field by stacking simulated \hat{v}_a values on real galaxy locations:

$$X_a^{\text{sim}}(\boldsymbol{\theta}) = \sum_{i \in \text{gal}} W_i \hat{v}_a^{\text{sim}}(\mathbf{x}_i) \delta^2(\boldsymbol{\theta} - \boldsymbol{\theta}_i), \quad (\text{B1})$$

and decompose into gradient/curl modes $X_{\ell m}^{G,\text{sim}}, X_{\ell m}^{C,\text{sim}}$.

- When we compare the gradient auto power spectrum $C_\ell^{GG,\text{sim}}$ of the simulations to the data, we find that they differ by an ℓ -independent constant (for $\ell \gtrsim 2500$):

$$C_\ell^{GG,\text{data}} = A^2 C_\ell^{GG,\text{sim}} \quad \text{where } A = \begin{cases} 1.18 & \text{NGC main sample} \\ 1.08 & \text{NGC extended sample} \\ 1.36 & \text{SGC main sample} \\ 1.61 & \text{SGC extended sample} \end{cases} \quad (\text{B2})$$

We attribute $A > 1$ to imaging systematics in DESILS, which are larger in the SGC due to the boundary between the DES and the non-DES parts of the survey. (We checked that if we restrict to the non-DES subset of the SGC, then the value of A decreases to a value which is similar to the NGC.)

- We correlate $X_{\ell m}^{G,\text{sim}}$ with the ACT data (not an ACT simulation), obtaining $C_\ell^{TG,\text{sim}}$. We bin the power spectrum $C_\ell^{TG,\text{sim}}$ in ℓ (as in Eq. 22) obtaining a length- N_b vector s_b . We then estimate the binned power spectrum covariance $C_{bb'}$ from the simulations, assuming zero off-diagonal covariance:

$$C_{bb'} = \text{Var}(As_b) \delta_{bb'}, \quad (\text{B3})$$

where the variance is taken over Monte Carlo simulations s_b , and the factor A rescales the simulations to match the data (note that rescaling $s_b \rightarrow As_b$ is equivalent to rescaling $X_a \rightarrow AX_a$ at field level).

When we assign error bars in this way, we find excellent agreement with the empirical method (Eq. 23) in the main paper. The agreement between these very different methods is a strong check. Note that both methods account (in different ways) for imaging systematics, which increase the size of the error bars. In the simulation-based method in this appendix, we introduce the factor A to rescale the simulations to match the data. In the empirical method in the main paper, we use the scatter (between values of ℓ) in the measured C_ℓ^{TG} , which automatically includes both statistical and systematic errors.

Appendix C: Numerical CMB foreground bias in a simplified simulation pipeline

In this section, we describe the simplified simulation pipeline that was used in §VIB to estimate CMB foreground biases to our moving-lens pipeline. Our pipeline is based on Quijote simulations [30], and uses a “snapshot” geometry instead of an evolving lightcone geometry: large-scale structure fields are defined in a 3-d periodic box at a fixed time ($z_* = 1$). We choose $z_* = 1$ for convenience, even though we use $z_* = 0.734$ in the main body of the paper, since Quijote snapshots are only available at a few specific redshifts. The CMB is a 2-d flat-sky field obtained by projecting onto one periodic face of the box.

Each Quijote simulation consists of a matter distribution (512^3 particle positions and velocities) and a halo catalog (positions, velocities, and halo masses) in a box with side length $L_{\text{Quijote}} = 1 h^{-1} \text{Gpc}$. The halo catalog contains halos with ≥ 20 particles ($M \geq 2 \times 10^{13} M_\odot$).

Throughout this appendix, we make frequent use of the tSZ/CIB halo model and code³ from [31]. All foreground model inputs below (e.g. the tSZ profile $y_l(M, z)$ in Eq. (C1), or the CIB power spectrum dC_l^{CIB}/dz in Eq. (C4)) are computed using this code.

³ https://github.com/abhimaniyar/halomodel_cib_tsz_cibxtsz

1. Toy tSZ model

Nearly 100% of the tSZ signal comes from halos that are resolved by Quijote ($M \geq 2 \times 10^{13} M_\odot$). Therefore, our toy tSZ model uses the Quijote halo catalog at $z_* = 1$, rather than the matter snapshot. We simulate the y -map by “painting” an azimuthally symmetric profile $y_l(M)$ at each halo location:

$$y(\mathbf{l}) = \sum_{i \in \text{halos}} y_l(M_i) e^{-i\mathbf{l} \cdot \boldsymbol{\theta}_i} \quad (\text{C1})$$

where $y_l(M)$ is the mass-dependent tSZ angular profile from [31], and $\boldsymbol{\theta}_i = x_i^\perp / \chi_*$ is the angular location of halo i .

One minor issue here: the Quijote halo catalog uses friends-of-friends masses M_{FOF} , whereas the tSZ profiles from [31] use M_{500c} . To convert $M_{\text{FOF}} \rightarrow M_{500c}$, we assume $M_{\text{FOF}} \approx M_{\text{vir}}$, that halo profiles are NFW, and that halo concentrations are given by the Duffy08 fitting function [43]. As a check, we verified that after converting $M_{\text{FOF}} \rightarrow M_{500c}$, the halo mass function dn/dM_{500c} of the Quijote sims agrees well with the code from [31].

To compute Eq. (C1) efficiently, we use the following algorithm. Let $u_l(M) \equiv y_l(M)/y_0(M)$ be the dimensionless profile (normalized to $u_l = 1$ at $l = 0$). We precompute $u_l(M)$ on a grid $\{M_a\}_{1 \leq a \leq 10}$ of ten M -values, uniformly spaced in $\log(M)$. We then linearly interpolate (in $\log M$) to the mass M_i of each halo:

$$u_l(M_i) \approx \sum_a W_{ia} u_l(M_a) \quad (\text{C2})$$

where W_{ia} is an N_{halo} -by-10 sparse matrix of linear interpolation weights.

The point of this linear interpolation is that it allows Eq. (C1) to be computed efficiently with 10 FFTs. Plugging Eq. (C2) into Eq. (C1) and doing a little algebra, we can write $y(\mathbf{l})$ in the form:

$$y(\mathbf{l}) \approx \sum_a u_l(M_a) Z_a(\mathbf{l}) \quad \text{where } Z_a(\mathbf{l}) \equiv \sum_i y_0(M_i) W_{ia} e^{-i\mathbf{l} \cdot \boldsymbol{\theta}_i} \quad (\text{C3})$$

Each map $Z_a(\mathbf{l})$ can be computed by gridding the halo catalog into a real-space map, with per-object weight $y_0(M_i) W_{ia}$, and then taking an FFT.

2. Toy CIB model

Most of the CIB signal comes from halos that are not resolved by Quijote (in contrast to the preceding tSZ case). Therefore, our toy CIB model will use the matter snapshot of the Quijote simulations, not the halo catalog. We simply assume that CIB emission is proportional to the total matter field, via an l -dependent factor, which is chosen to give a realistic power spectrum C_l .

In more detail, for each Quijote simulation, we project the matter field from 3-d to 2-d, obtaining a 2-d matter field $\rho_m^{2d}(\boldsymbol{\theta})$. Then, we model $T_{\text{CIB}}(\boldsymbol{\theta})$ by applying an l -dependent rescaling to match a “target” CIB power spectrum:

$$T_{\text{CIB}}(\mathbf{l}) = \left(\frac{C_l^{\text{target}}}{C_l^{\rho_m^{2d}}} \right)^{1/2} \rho_m^{2d}(\mathbf{l}) \quad \text{where } C_l^{\text{target}} \equiv \left(\frac{dC_l^{\text{CIB}}}{dz} \right)_{z=z_*} H(z_*) L_{\text{Quijote}} \quad (\text{C4})$$

Here, dC_l^{CIB}/dz is the predicted CIB power spectrum per unit redshift, and C_l^{target} is the CIB power spectrum due to a “shell” of large-scale structure whose thickness matches the Quijote box size L_{Quijote} .

3. Simplified moving-lens pipeline

For each Quijote simulation, we run a simplified moving-lens pipeline which follows the steps from our main pipeline (§III), adapted to the snapshot geometry. Since the input to our pipeline is a galaxy field, we use the Quijote halo catalog (i.e. we assume one central galaxy per halo). The number density $n_g = 5.9 \times 10^{-5} \text{ Mpc}^{-3}$ is similar to DESILS ($n_g = 1.3 \times 10^{-4}$ for the main LRG sample, or $n_g = 3.3 \times 10^{-4}$ for the extended sample).

First, we construct a 3-d velocity reconstruction $\hat{v}_j(\mathbf{x})$ from the galaxy catalog:

$$\rho_g(\mathbf{x}) = \sum_{i \in \text{gal}} \delta^3(\mathbf{x} - \mathbf{x}_i) \quad \hat{v}_j(\mathbf{k}) = (ik_j)U(k)\rho_g(\mathbf{k}), \quad (\text{C5})$$

where the Wiener filter $U(k)$ is defined by:

$$U(k) = \begin{cases} \frac{faH}{k^2 b_g} \frac{b_g^2 P_{mm}(k)}{b_g^2 P_{mm}(k) + 1/n_g} & \text{if } k < k_{\text{max}}, \\ 0 & \text{otherwise.} \end{cases} \quad (\text{C6})$$

Note that the definition (C5) of ρ_g does not include random subtraction, since our snapshot geometry does not include a sky cut or time evolution. Second, we construct a 2-d vector field $X_a(\boldsymbol{\theta})$ by:

$$X_a(\boldsymbol{\theta}) = \sum_{i \in \text{gal}} \hat{v}_a(\mathbf{x}_i) \delta^2\left(\boldsymbol{\theta} - \frac{\mathbf{x}_i^\perp}{\chi_*}\right). \quad (\text{C7})$$

Third, we take the cross power spectrum C_l^{TG} between the CMB foreground map (either $T_{\text{tSZ}}(\boldsymbol{\theta})$ or $T_{\text{CIB}}(\boldsymbol{\theta})$) and the gradient mode X_G of the field X_a . We convert from C_l^{TG} to $P_{g\Psi}(k)$ using:

$$l b_l P_{g\Psi}(l/\chi_*) = \frac{1}{\mathcal{N}} C_l^{TG} \quad \text{where } \mathcal{N} = \frac{T_{\text{CMB}}}{\Omega_{\text{sky}} \chi_*^3} \sum_{\text{gal}} (v_{\perp}^{\text{true}} \cdot \hat{v}_{\perp}), \quad (\text{C8})$$

where $\Omega_{\text{sky}} = L_{\text{Quijote}}^2/\chi_*^2$ is the survey area in steradians, and we average $P_{g\Psi}(k)$ over 1000 Quijote simulations. The mean $P_{g\Psi}(k)$ curves, representing foreground bias to the moving-lens pipeline, are shown in Figure 6.

The ‘‘moving lens signal’’ curves in Figure 6 were obtained separately, by computing $P_{g\Psi}(k)$ using the halo model. We assume NFW matter profiles and choose parameters b_g, \bar{n} appropriate for the $z = 1$ Quijote snapshots. (Note that these signal curves are slightly different from the ones shown elsewhere in the paper, since Quijote parameters are slightly different from DESILS parameters.)

The simplified pipeline in this section could be extended to include many real-world complications, including the non-snapshot geometry (angular mask and time evolution), RSDs and photo- z errors, and more complex CMB foreground models. We plan to explore these extensions in future work.